Title: The BR-body proteome contains a complex network of protein-protein and protein-RNA interactions

Authors: Nandana, V.[1]#, Rathnayaka-Mudiyanselage, I.W.[1,2]#, Muthunayake, N.S.[1*], Hatami, A.[3] Mousseau, C.B.[4], Ortiz-Rodríguez, L.A.[5], Vaishnav, J.[3$], Collins, M.[6], Gega, A.[1&], Mallikaarachchi, K.S.[1], Yassine, H.[1], Ghosh, A.[1], Biteen, J.S.[5], Zhu, Y.[3], Champion, M.M.[4], Childers, W.S.[6], Schrader, J.M.[1]

[1]Wayne State University, Department of Biological Sciences, Detroit, MI

[2]Wayne State University, Department of Chemistry, Detroit, MI

[3]Wayne State University, Department of Chemical Engineering and Materials Science, Detroit, MI

[4]University of Notre Dame, Department of Chemistry, Notre Dame, IN

[5]University of Michigan, Department of Chemistry, Ann Arbor, MI

[6]University of Pittsburgh, Department of Chemistry, Pittsburgh, PA

[#]These authors contributed equally

[&]Current affiliation: University of Toledo Medical School

[$]Current affiliation: University of Massachusetts-Amherst

*Current affiliation: Wayamba University of Sri Lanka, Faculty of Medicine, Department of Biochemistry

Corresponding Author: Schrader@wayne.edu

Highlights

1. BR-body proteomics identified 111 proteins enriched in BR-bodies.
2. BR-bodies associate with an interconnected network of RNP condensates.
3. BR-body condensation is modulated by its interaction network.
4. RNA is required for rapid BR-body condensation.

Abstract

Bacterial RNP bodies (BR-bodies) are non-membrane-bound structures that facilitate mRNA decay by concentrating mRNA substrates with RNase E and the associated RNA degradosome machinery. However, the full complement of proteins enriched in BR-bodies has not been defined. Here we define the protein components of BR-bodies through enrichment of the bodies followed by mass spectrometry-based proteomic analysis. We found 111 BR-body enriched proteins, including several RNA binding proteins, many of which are also recruited directly to *in vitro* reconstituted RNase E droplets, showing BR-bodies are more complex than previously assumed. While most BR-body enriched proteins that were tested cannot phase separate, we identified five that undergo RNA-dependent phase separation *in vitro*, showing other RNP condensates interface with BR-bodies. RNA degradosome protein clients are recruited more strongly to RNase E droplets than droplets of other RNP condensates, implying that client specificity is largely achieved through direct protein-protein interactions. We observe that some RNP condensates assemble with preferred directionally, suggesting that RNA may be trafficked through RNP condensates in an ordered manner to facilitate mRNA processing/decay, and that some BR-body associated proteins have the capacity to dissolve the condensate. Finally, we find that RNA dramatically stimulates the rate of RNase E phase separation *in vitro*, explaining the dissolution of BR-bodies after cellular mRNA depletion observed previously. Altogether, these results suggest that a complex network of protein-protein and protein-RNA interactions controls BR-body phase separation and RNA processing.

Introduction

Biomolecular condensates have been shown to be an important mode of subcellular organization in eukaryotes and bacteria[1–3]. As bacteria often lack membrane-bound organelles, biomolecular condensates may provide a generalized strategy for their subcellular organization. Indeed, many bacterial biomolecular condensates have been recently identified in various species, including BR-bodies, signaling condensates, DNA replication condensates, RNApol condensates, Hfq condensates, Rubisco condensates, etc.[4–10]. Biomolecular condensates typically assemble through the physical process of phase separation, which involves association of macromolecular scaffolds and segregation of other cellular components, ultimately leading to distinct non-membrane bound structures[11]. Recent analyses of condensate physical properties appear to be consistent with a model of percolation-coupled phase separation, which includes both associative interactions as well as segregative[12], leading to phase separation[13]. Macromolecules that have the capacity to phase separate are referred to as scaffolds, which generally provide a platform for the multi-valent interactions that lead to phase separation. Molecules that are recruited to condensates but cannot phase separate themselves are called clients[14]. A condensate's composition of scaffolds and clients determines its biochemical and cellular function. Importantly, molecules inside of condensates often show diffusive dynamics, suggesting biomolecular condensates facilitate the biochemical processes within them[15,16]. Several models have been proposed for how condensates might accelerate enzyme-catalyzed processes, including increasing reaction rates by raising the local concentration of substrates and enzymes, increasing reaction specificity by the selective recruitment of certain substrates and avoidance of others, and increasing reaction completion by preventing the release of pathway intermediates[17–19]. Conversely, biomolecular condensates have also been proposed to sequester substrate molecules from their enzymes, leading to a reduction in reaction rates[20,21]. Therefore, it is important to identify the essential molecular components of the condensate to determine the biochemical consequences of biomolecular condensate organization.

Despite advances in biomolecular condensate biochemistry, many *in vitro* studies have focused on purified scaffolds, and often lack the full suite of molecules identified to interact *in vivo*. This is potentially problematic, as proteomic/transcriptomic investigations in eukaryotes have revealed that biomolecular condensates are enriched in hundreds of different molecular species that may alter their biochemical or cellular functions. For example, P-bodies have been found to contain >125 proteins and >6000 RNA transcripts[22], and importantly appear to help concentrate mRNA decay enzymes (including decapping enzymes, LSM proteins, Xrn1 nuclease, deadenylases, etc.) together with decapped and translationally repressed mRNAs. Stress granules have been found to contain >300 proteins and >1800 RNA transcripts[23–25], often including a partially overlapping set of components with P-bodies[22,26], yet the differences in composition and slower dynamics[27] suggests that these structures likely have distinct functions. Through careful quantitative measurements, the core set of P-body proteins has recently been reconstituted *in vitro*, with similar dynamic properties[28]. In bacteria, BR-bodies were found to be enriched in long, poorly translated cellular mRNAs and sRNAs, a class of translational repressors, together with the RNA degradosome proteins[4,29]. Therefore, it was assumed that this structure might have a small set of protein clients that could be amendable to full *in vitro* reconstitution [27]; however, the full complement of proteins in BR-bodies has not been identified .

To define the proteome of *Caulobacter crescentus* BR-bodies, we performed cellular enrichment by differential centrifugation[30] followed by quantitative liquid chromatography tandem mass spectrometry

(LC-MS). Similar to eukaryotic condensates, we identified over 100 proteins that were enriched in BR-bodies. Enriched proteins tended to localize into foci *in vivo* and enter RNase E condensates *in vitro*, suggesting many are likely direct clients of RNase E, the main scaffold of the BR-body. While most enriched proteins do not assemble into biomolecular condensates *in vitro*, we identified five BR-body associated proteins that can undergo phase-separation (phase separate without RNase E), suggesting they form distinct RNP condensates in the cell that interact with RNase E. By assaying the pairwise ability of each scaffold protein to mix with the others, we observed that some pairs of scaffolds have strong associations, and that certain pairs show preferred directional recruitment, which likely impacts RNP assembly order, leading to heterogenous RNP condensates *in vivo*. We also identified two proteins that can dissolve BR-bodies both *in vivo* and *in vitro*, suggesting that they may negatively regulate the cell's ability to assemble BR-bodies. Despite the identification of many BR-body associated proteins, the RNA degradosome proteins are the only proteins identified that stoichiometrically bind to RNase E[31] and that are uniformly colocalized with RNase E foci *in vivo*, suggesting a minimal BR-body may be possible to reconstitute. Minimal BR-body phase separation was kinetically stimulated by RNA and showed similar RNase E FRAP dynamics to RNase E-RNA droplets. Overall, this suggests that BR-bodies have similar complex interaction network to eukaryotic RNP condensates, and the reconstitution of the "core" minimal BR-body components provides an exciting framework to begin assessing their biochemical functions and how they might be altered by the addition of BR-body associated proteins.

Results

Characterization of the BR-body proteome by LC-MS Proteomics

To define the *C. crescentus* BR-body associated proteome, BR-body enrichment was performed as in[30] and subjected to bottom-up proteomics preparation and analysis (Fig 1A, Table S1). BR-body enriched samples were compared to a mock treated lysate of a mutant that is unable to assemble BR-bodies due to the deletion of the C-terminal IDR of RNase E[30]. 100 μg protein was prepared in triplicate for either condition and converted into peptides via enzymatic digestion using S-Traps[32]. Each sample was analyzed by LC-MS in technical triplicate. Peptide-spectral matching, protein inference, and Label Free Quantification (LFQ) were performed using FlashLFQ in MetaMorpheus[33]. Data were filtered to an FDR of 1.0% and exported as text for analysis. Using these parameters, a total of 1079 proteins were identified in both samples, and the ratio of signal in the BR-body enriched sample (JS299) over the negative control (JS221) was plotted (Fig 1B). 111 proteins were identified to be enriched in BR-bodies. These enriched proteins had Log2 BR-body enrichment value of >1 (>2-fold enrichment) with a >95% confidence interval (resulting p-values subject to Benjamini-Hochberg correction) or were identified in all three biological replicates in BR-body enriched samples but were not detected in the negative control. These enriched proteins were predominantly cytoplasmic, while proteins derived from other cellular compartments were depleted, suggesting reasonable enrichment of BR-bodies occurred in the sample. In addition, we observed significantly higher scores for known RNase E associated proteins, while proteins that interact with polar biomolecular condensates were highly depleted (Fig 1B), suggesting that the enrichment was likely not contaminated with all cellular condensates. GO-term analysis of BR-body enriched proteins revealed RNA binding, ATP binding, GTPase activity, and RNA degradation functionalities (Fig 1B).

To validate whether BR-body enriched proteins localize into BR-bodies *in vivo*, we examined the ability of enriched proteins to localize into foci *in vivo*, the foci's dependence on RNase E expression, and

124 the proteins' colocalization with BR-bodies. To comprise the set of BR-body enriched proteins, we chose
125 proteins that are part of the *C. crescentus* RNA degradosome [31,34], proteins that associate with RNase E
126 in the cold [35], and proteins that are known to have a role in RNA processes. We selected proteins with
127 no known role in RNA processes (DnaK and FabG) as a negative control. In addition, we also chose a set
128 of proteins that were not enriched in BR-bodies, but function in RNA decay. We expressed each protein
129 with a YFP tag from the vanillate locus (Fig S1) and determined the average number of foci per cell (Fig
130 2A). Importantly, even when expressed at very high levels in *Caulobacter*, YFP is not sufficient to form
131 foci *in vivo*[36]. Interestingly, 7/12 proteins from the BR-body enriched set assembled into foci in the
132 cells, while only 2/10 proteins (RNase HI and MetK) from the negative control set showed foci. Of the
133 5/12 proteins that were enriched but did not form foci, it is possible that the C-terminal YFP tag
134 interfered with their ability to form foci, as SmpB, which was found to form foci by
135 immunofluorescence[37], did not form foci when fused to YFP.

136 To test whether the observed foci were BR-bodies, we examined the colocalization of foci with
137 either the core BR-body scaffold RNase E or its direct binding partner Aconitase[4]. To examine
138 colocalization, we drew a line across the foci of each protein, and then correlated the intensity between
139 this channel and that of the BR-body marker (Fig 2B). As a negative control, we included PopZ, a protein
140 that can form a polar biomolecular condensate involved in cell signaling [38]. We could not visualize
141 PNPase-YFP together with RNase E-mCherry or Aconitase-mCherry and we noticed very slow growth
142 rates of this strain. We found that for the core degradosome proteins Aconitase and RhlB [31], foci were
143 uniformly colocalized with RNase E in all cases (average Correlation = 0.94 Aconitase, 0.92 RhlB), while
144 RNase E foci did not correlate with PopZ foci (average Correlation = 4.8×10^{-3}). We found that RNase D1,
145 RhlE, Rho, and Hfq showed significant but heterogenous colocalization with BR-bodies (average
146 Correlation = 0.32 RNase D1, 0.39 RhlE, 0.72 Rho, 0.52 Hfq), while BR-body depleted proteins RNase H1
147 and MetK showed no correlation (average Correlation = 3.1×10^{-2} MetK, 6.1×10^{-2} RNase H1), similar to
148 the PopZ control, suggesting they are indeed not enriched in BR-bodies. Interestingly, RNase D1 was
149 found to be RNase E associated[34] but was depleted in the BR-body proteomics data, while RNase D2 was
150 found to be highly enriched in BR-bodies, suggesting that they may be interchangeable. We observed
151 that RNase D1-YFP appeared to be localized to the inner membrane, suggesting that perhaps it was lost
152 upon the initial membrane pelleting step of the BR-body enrichment procedure. In line with this
153 hypothesis, we observed significant colocalization between RNase D1-YFP and RNase E-mCherry in live
154 cells (Fig 2B). We did not observe foci of RNase D2-YFP (Figs 2A, S1), suggesting that either it is not-
155 enriched in BR-bodies, or that the YFP tag is disrupting its localization. The heterogeneity of RNase D1,
156 RhlE, and Hfq suggests that they are present in a subset of BR-bodies, suggesting that some BR-bodies
157 have different compositions or protein clients.

158 Identification of BR-body associated scaffolds that condense independent of 159 RNase E

160 Since RNase E is necessary and sufficient to form BR-bodies[4], we tested whether RNase E was
161 required for BR-body enriched proteins to form foci (Fig 2C). Because RNase E is essential, we used an
162 RNase E depletion strain where the sole copy of RNase E is under control of the xylose promoter[4]. While
163 most proteins maintained similar YFP fluorescence in the RNase E depletion strain, RhlB-YFP, Aconitase-
164 YFP, PNPase-YFP, and RNase H1-YFP were expressed at levels that were too low to detect (Figs 2C, S2).
165 To overcome this low Aconitase-YFP expression, we utilized a strain in which Aconitase-YFP is present at
166 its native loci in the same xylose-dependent RNase E depletion strain[4]. While most of the strains would

saturate cultures overnight, PNPase-YFP expression was toxic in the depletion strain background, leading to extremely slow cell growth in liquid culture, so we were unable to assay this strain. As a control we included PopZ, which is known to form an independent biomolecular condensate in *C. crescentus*[6]. For Aconitase, RNase D1, Hfq, and Rho, fluorescent foci levels dropped significantly upon RNase E depletion, suggesting that these proteins require RNase E to assemble into foci. Interestingly, for MetK and RhlE, foci levels were unchanged or higher upon RNase E depletion, similar to the PopZ control, suggesting that these two proteins assemble into foci independent of RNase E. To examine whether these enriched proteins impact RNase E phase separation, we measured RNase E-GFP foci in strains where the enriched proteins were deleted. Due to Aconitase, RNase D1, and Rho being essential, we only inserted RNase E-GFP into RhlB and hfq deletion strains, or an RhlE disruption mutant strain. We observed no significant difference in the number of RNase E-GFP foci in these strains (Fig 2D), suggesting that RhlB, RhlE, and Hfq do not impact BR-body phase separation *in vivo*.

As MetK and RhlE proteins were found to form RNase E-independent foci *in vivo*, we tested whether these proteins could directly self-assemble into condensates *in vitro*. In addition to MetK and RhlE, we also included several proteins from the BR-body enrichment dataset and also proteins known to interact with RNase E (Figs 3, S3A). Purified proteins were incubated at their estimated *in vivo* concentrations[39] with or without 20 ng/µL of *C. crescentus* total RNA. We found that RhlE, DEAD, Hfq, MetK, and FabG all assembled RNA-stimulated condensates *in vitro* (Figs 3A, B), suggesting that these proteins are scaffolds that can drive RNA-dependent condensation. Conversely, most of the proteins tested, including PNPase, Aconitase, RhlB, RNase D1, Ribosomal protein S1, NudC, RppH, Rho, NusG, DnaK, and Tyrosyl tRNA synthetase (TyrRS) did not undergo phase separation regardless of the presence of RNA (Fig S3B). Consistent with the phase-separation of RhlE, DEAD, and Hfq, the homologous proteins from *E. coli* were recently found to assemble into condensates *in vitro* or when overexpressed *in vivo*[7,40]. To test whether these structures are condensates, we performed high salt and RNase treatment of pre-formed condensates (Fig 3C), and in each case the condensates were strongly dissociated, suggesting multivalent electrostatic interactions with RNA are likely important for driving phase separation, like in RNase E condensates[4]. RhlE, DEAD, and Hfq contain intrinsically disordered regions (IDRs) (Fig 3A) that have been characterized as important for their *E. coli* homologues' ability to form droplets[40,41]. Prior experiments also showed that the IDR of RNase E was both necessary and sufficient for phase separation[4]. To test the function of these IDRs on phase-separation, we deleted the IDRs of *C. crescentus* RhlE, DEAD, and Hfq and tested their ability to phase-separate. We found that for Hfq and DEAD, the IDR deletions showed reduced phase separation, while for RhlE the IDR deletion was indistinguishable from wild-type (Fig S3C). We did not include FabG and MetK in these experiments as no disordered regions were predicted in their sequences (Fig 3A). Overall, this suggests that for some scaffold proteins, IDRs positively influence but are not strictly required for phase separation.

A complex network of molecular interactions regulates RNP condensation

To better understand which proteins can enter BR-bodies, we selected a set of 18 proteins (Fig S3A) to test further for their recruitment directly into RNase E droplets (Fig 4A). We picked proteins enriched from the BR-body proteomics dataset with known RNA processing roles, proteins known to have protein-protein interactions with RNase E but not detected in the BR-body proteomics experiment, as well as negative control proteins with low BR-body enrichment and no known/predicted interaction with RNase E. In these experiments RNase E and RNA were mixed to form an RNase E condensate, followed by incubation with a Cy5-labeled test protein. The partition coefficient was calculated based

210 on the Cy5 fluorescence (Figs 4B, S4A). We observed that the core RNA degradosome proteins PNPase,
211 Aconitase, RhlB, and RNase D1 all had positive partition coefficients ranging from 2.7 to 4.7, showing
212 that they enter RNase E condensates, while our negative controls BSA and SpmX, which forms a polar
213 signaling condensate[6], did not enter the RNase E condensate and yielded a partition coefficient near 1,
214 indicating no enrichment. We also identified partition coefficients at similar levels to the core
215 degradosome proteins for RhlE, DnaK, and FabG. In contrast, NudC, RppH, Rho, NusG, and TyrRS all had
216 partition coefficients close to 1, similar to the negative controls BSA and SpmX (Fig 4B). The low
217 partition coefficients for RppH and NudC are consistent with their lack of enrichment in the BR-body
218 proteomics assay; however, Rho, NusG, and TyrRS all had significant enrichment in the BR-body
219 proteomics data, suggesting that they may enter BR-bodies indirectly through another protein. Despite
220 the finding that many proteins were able to enter BR-bodies, none of these proteins altered the
221 partition coefficient of RNase E (Fig S4B), suggesting that most BR-body associated proteins tested did
222 not dramatically influence RNase E's condensation.

223 Next, we tested which BR-body associated proteins might induce condensation in the absence
224 of RNA (Fig S5A). We assessed the ability of BR-body associated proteins to stimulate RNase E
225 condensation at their *in vivo* concentrations[39]. PNPase, RhlB, and RhlE stimulated RNase E condensates
226 rather robustly in the absence of RNA (Fig S5A). In addition, FabG and Hfq stimulated irregularly shaped
227 condensates in the absence of RNA, while Aconitase, RNase D1, NudC, RppH, Rho, NusG, DnaK, TyrRS,
228 ribosomal protein S1, and MetK did not stimulate RNase E condensation (Fig S5A). This suggests that a
229 subset of BR-body associated proteins can stimulate RNase E condensation independent of RNA.

230 Interestingly, we observed that the addition of ribosomal protein S1 (RpsA) or MetK, which were
231 not BR-body enriched (Table S1) but were previously found to associate with RNase E via co-
232 immunoprecipitation (co-IP)[35], could dissolve RNase E droplets *in vitro* (Figs 4A,5A). Ribosomal protein
233 S1 could only dissociate the droplets if the condensates contained total RNA, while MetK showed strong
234 dissolution if RNase E was condensed with RNA or with the protein PNPase. To test whether the
235 differences between S1 and MetK were related to their inherent RNA binding interactions, we examined
236 their apparent binding on 9S rRNA, a known RNase E substrate[31]. Based on native gel shifts, we found
237 that ribosomal protein S1 bound RNA with tighter apparent affinity than MetK (Fig 5B). The tighter
238 apparent affinity with RNA may explain why ribosomal protein S1 preferentially dissolves RNase E
239 condensates in the presence of RNA. We also used an affinity pull-down assay to test MetK and
240 ribosomal protein S1's association with MBP-RNase E. Indeed, as compared to the core BR-body protein
241 Aconitase, which is thought to stoichiometrically bind to RNase E[30], we found that MetK showed less
242 pull-down than Aconitase, while ribosomal protein S1 showed no detectable retention (Figs 5C, S5B).
243 Overall, these data suggest that MetK dissociates BR-bodies through interactions with the RNase E
244 protein (Fig 5). Because MetK showed a weak pull-down signal, we tested the pairwise interaction
245 between MetK and RNase E in a bacterial two-hybrid assay where each protein was expressed
246 recombinantly in *E. coli*[42] and found that MetK and RNase E do interact *in vivo* (Fig 5D). In the bacterial
247 two-hybrid, we found that Aconitase-T18/RNase E-T25 and MetK-T18/RNAse E-T25 interacts similarly to
248 the T18-Zip/T25-Zip positive control, and RNase E-T25/S1-T18 showed no *lacZ* signal, similar to the
249 T18/T25 negative control. To examine whether the observed *in vitro* dissolution effect of S1 and MetK
250 on BR-bodies is relevant *in vivo*, we inserted the ribosomal protein S1 *rpsA* and *metK* genes into the
251 pBXMCS-2 overexpression vector[43] and transformed the plasmid into a strain harboring a tagged BR-
252 body marker (Aconitase-mCherry)[4]. We observed *in vivo* that both MetK and ribosomal protein S1

253 overexpression strongly reduced Aconitase-mCherry foci (Fig 5E), confirming that their dissolution of BR-
254 bodies observed *in vitro* can also occur *in vivo*.

255 Some BR-body enriched proteins were able to assemble into RNP condensates independent of
256 RNase E (Fig 3B), but the client specificity of these RNP condensates is unknown. Because the RNA
257 degradosome client proteins are known to be stoichiometrically bound to RNase E via direct protein-
258 protein interaction sites[31,35] and show strong colocalization with BR-bodies (Fig 2B), we tested the
259 specificity of each driver/scaffold to each core RNA degradosome protein labeled with Cy5 dye (Fig 6A).
260 We observed a larger partition coefficient for all Cy5 degradosome clients to RNase E condensates as
261 compared to the other scaffolds/drivers (Figs 6A, S5B), suggesting that the degradosome proteins have a
262 specificity for entering RNase E condensates, likely through their direct protein-protein interactions with
263 RNase E.

264 Next, the miscibility of the drivers/scaffolds of each single RNP condensate was examined (Fig 6B).
265 First, we pre-formed a condensate using an unlabeled scaffold and then added in a Cy5-labeled scaffold
266 in all pairwise combinations and assayed the partition coefficients. We induced condensation in the
267 presence or absence of RNA to test the RNA dependency of each interaction. In the presence of RNA,
268 we assayed condensate formation using the predicted *in vivo* protein concentrations[39], and in the
269 absence of RNA, condensates were stimulated by increasing the protein concentration above its *in vivo*
270 concentration. For the RNase E condensate, we observed similar recruitment of other scaffolds
271 regardless of whether the condensates were formed with RNA or protein only (Figs 6B, S5C). The
272 partition coefficients for these scaffolds into RNase E condensates correlated with the BR-body
273 enrichment measured previously. RhlE was recruited most strongly into the RNase E condensate (11
274 partition coefficient) and had the highest observed BR-body enrichment (10 fold). RhlE was followed by
275 Hfq (7.5 partition coefficient, 3.2 BR-body enrichment), FabG (3.8 partition coefficient, 2.2 fold BR-body
276 enrichment), and DEAD (1.5 partition coefficient, 1.6 fold BR-body enrichment). RhlE was recruited
277 strongly into other RNP condensates, with partition coefficients ranging from 4.3 to 11, while the other
278 scaffolds were recruited poorly into RhlE-RNA condensates, with partition coefficients ranging from 1.5
279 to 2.5. In the absence of RNA, RhlE strongly recruited RNase E (12 partition coefficient) or DEAD (9.8
280 partition coefficient) while Hfq and FabG maintained similar partition coefficients (Fig S5C). DEAD
281 condensates showed strong recruitment of RhlE and lower recruitment of the other scaffolds, with
282 subtle changes in the presence or absence of RNA. RhlE and FabG were similarly recruited to Hfq
283 condensates regardless of the presence of RNA. RNase E dissolved Hfq-RNA condensates while Hfq
284 protein-only condensates strongly recruited RNase E (6.9 partition coefficient). DEAD was recruited at a
285 low level in Hfq-RNA condensates (1.8 partition coefficient) and dissolved Hfq-only condensates. FabG
286 condensates only formed in the presence of RNA and showed the strongest recruitment of RhlE (7.4
287 partition coefficient) and Hfq (3.4 partition coefficient). In summary, the scaffold proteins that assemble
288 diverse RNP condensates show specificity of recruitment, suggesting that some RNP condensates can
289 intermix, while others likely do not.

290 The asymmetric recruitment/dissolution (Fig 6B) and specificity of clients (Fig 6A) observed may
291 help shape the composition of the heterogeneous RNP condensates observed in the cell (Fig 2B). We
292 chose to study the RhlE-RNase E pair further because it showed the strongest directional recruitment in
293 the presence of RNA (Fig 6B). Specifically, RhlE was recruited robustly into RNase E droplets, but RNase E
294 was poorly recruited into RhlE droplets. First, we altered the order of addition of RhlE and RNase E
295 before triggering phase separation (Fig 6C). If the proteins were mixed before condensation with RNA,

296 we observed that RNase E and RhlE mix uniformly. However, when each protein was pre-assembled
297 into a condensate with RNA before mixing both RNP condensates together, we observed that RNase E
298 and RhlE condensates did not readily mix (Fig 6C). This contrasts with the prior observation that free
299 RhlE readily entered RNase E condensates (Fig 6B), suggesting that the order of assembly influences the
300 composition of RNase E and RhlE condensates.

301 To examine the order of RNase E and RhlE condensate formation *in vivo*, we took time-lapse
302 movies of RhlE and RNase E foci formation in cells. As a positive control, we observed that RNase E-YFP
303 and the core degradosome protein Aconitase-mCherry foci appear simultaneously (Fig 6D, S6A) with
304 uniform colocalization. When BR-bodies appear first, as indicated by Aconitase-mCherry foci, we
305 regularly observed RhlE-YFP signal within these foci (Fig 6D), consistent with the ability of RNase E
306 condensates to recruit RhlE *in vitro* (Fig 6B). In contrast, RhlE-YFP foci that appeared first generally
307 lacked a colocalized Aconitase-mCherry focus, consistent with the lack of *in vitro* recruitment of RNase E
308 by RhlE (Fig 6B). Taken altogether, these observations suggest that the molecular interactions driving
309 RhlE and RNase E condensation control the ability of these condensates to co-assemble and mix both *in*
310 *vitro* and *in vivo*. To further test whether the material properties of RhlE and RNase E condensates
311 affect mixing, we performed *in vitro* FRAP on RhlE and RNase E droplets (Fig S6B). We observed that
312 RNase E rapidly recovers either in RNase E-RNA condensates or in mixed RNase E-RhlE-RNA
313 condensates, while RhlE showed little to no recovery in either RhlE-RNA condensates or RNase E-RhlE-
314 RNA condensates (Fig S6B). This suggests that the more dynamic exchange in RNase E droplets
315 compared to RhlE droplets contributes to the preferred directional RhlE to RNase E assembly/mixing
316 observed *in vitro* and *in vivo*.

317 As RNase E did not appear to readily enter other associated RNP condensates (Fig 6B), we
318 wanted to better understand the role of RNA and the associated degradosome proteins on RNase E
319 condensation. We therefore examined the kinetics of condensation via time-lapse microscopy (Fig 7A,
320 7B). This assay likely reflects the kinetic processes of phase-separation and surface wetting of the
321 microscope slide. When incubated alone at its predicted *in vivo* concentration, RNase E did not phase
322 separate *in vitro* even after long incubations of many minutes. The addition of RNA strongly stimulated
323 the rate of condensation, occurring on the sub-minutes timescale, consistent with the known
324 importance of RNA for RNase E condensation *in vivo* and in end-point *in vitro* assays[4,29]. When RNase E
325 was incubated at concentrations much higher than its *in vivo* concentration, it was able to phase
326 separate without RNA after many minutes, (Fig S7).

327 RNase E is known to scaffold the RNA degradosome protein complex, and the degradosome
328 proteins stoichiometrically bind to RNase E[31] and are homogeneously present with RNase E in BR-
329 bodies[4]. To test the effects of degradosome proteins on condensation kinetics, we added either PNPase
330 or the full set of core degradosome proteins (PNPase, Aconitase, RhlB, and RNase D1) to the
331 condensation assembly experiment. Upon the addition of PNPase or the full set of core RNA
332 degradosome proteins, RNase E still rapidly condensed on a sub-minute timescale that was accelerated
333 by the addition of RNA (Fig 7A). This suggests that the combined interactions with the RNA
334 degradosome proteins likely do not dramatically alter RNase E's condensation kinetics in the presence of
335 RNA. This may be due to the degradosome protein binding sites being located outside the Arg-rich RNA
336 binding sites in the C-terminal domain of RNase E[31]. As noted previously, we observed that the
337 degradosome protein PNPase was able to stimulate RNase E condensation *in vitro* in the absence of RNA
338 (Fig S5A). We therefore assayed the kinetics of RNase E and PNPase condensation in the absence of

339 RNA and found that the kinetics were dramatically slower than in the presence of RNA (Fig 7A). Overall,
340 this suggests that RNA provides the strongest kinetic stimulation of condensation, and the RNA
341 degradosome clients can provide a slight further enhancement of the rate of RNA-mediated
342 condensation.

343 To understand if RNA or degradosome protein interactions alter the mobility of molecules in the
344 condensed state, we performed FRAP experiments (Fig 7B, C). RNase E condensates lacking RNA had the
345 slowest recovery, at 2.4 min $\tau_{1/2}$, while the addition of RNA accelerated the FRAP recovery $\tau_{1/2}$ to 0.23
346 min. Interestingly, mobility was still fast upon the addition of PNPase and RNA or all of the
347 degradosome proteins and RNA, with recovery times similar to the RNase E with RNA sample ($\tau_{1/2}$ of 0.34
348 and 0.42 min, respectively). This suggests that the addition of RNA significantly increases the mobility of
349 RNase E condensates, regardless of the presence of degradosome clients. Interestingly, the addition of
350 RNase E and PNPase in the absence of RNA showed a recovery $\tau_{1/2}$ of 0.38 min. This suggests that, even
351 though the degradosome proteins do not dramatically stimulate the rate of condensation, degradosome
352 protein interactions likely do influence the mobility of RNase E within the droplets, either indirectly by
353 altering the structure of the CTD or directly by influencing multivalent protein-protein interactions in the
354 condensed state. Altogether, RNA appears to stimulate the rate of RNase E condensation, while the
355 recruitment of RNA or protein clients increases the mobility of RNase E within the condensate, which
356 may promote enhanced biochemical activity.

357 Discussion

358 **A complex protein interaction network impacts BR-body condensation and composition**

359 Analysis of the BR-body proteome revealed enrichment of >100 proteins of various biochemical
360 functions, suggesting that BR-bodies are more complex than previously assumed. We observed that a
361 subset of BR-body enriched proteins known to stoichiometrically assemble into the RNA degradosome
362 (RNase E, RhlB, Aconitase, and PNPase) appear to be uniformly enriched in BR-bodies *in vivo*[4] and
363 selectively recruited to RNase E condensates *in vitro* (Fig 6). This suggests that the RNA degradosome
364 likely composes the "core" set of proteins making up each BR-body. As observed for yeast P-bodies, a
365 set of "core" proteins that were found to be quantitatively enriched[27] and likely homogeneously
366 represented in these structures, were successfully reconstituted *in vitro* with similar dynamics
367 properties and stoichiometries identified[28]. An important future goal will be to define the role of BR-
368 body localization to each of the core enzymes involved in the RNA decay process. Indeed, in a two
369 protein BR-body system using only RNase E and PNPase, PNPase activity was observed to be directly
370 stimulated by condensation with RNase E[17], suggesting that the organization in BR-bodies may help to
371 stimulate RNA degradosome activity.

372 In addition to a uniformly enriched core of RNA degradosome proteins, we also found multiple
373 proteins that were heterogeneously localized with BR-bodies, including the DEAD box RNA helicase RhlE,
374 the transcription termination factor Rho, and the RNA chaperone Hfq. Although Rho was strongly
375 colocalized with RNase E foci *in vivo*, we found that only a subset of RNase E foci contained Rho signal
376 (Fig 2). RhlE and Hfq were both present in a subset of RNase E foci, and they could also form
377 independent foci *in vivo* that did not contain RNase E (Fig 2). Importantly, non-RNase E scaffolds that can
378 undergo heterotypic phase separation with RNA are enriched in BR-bodies, which suggests that many
379 cellular RNP condensates exist and interact with BR-bodies. Five proteins that interact with RNase E

380 were identified as scaffolds that can phase separate with RNA *in vitro*: RhlE, DEAD, Hfq, FabG, and MetK.
381 Together with the RNApol and Rho condensates identified previously[5,44], this suggests that bacteria
382 contain many RNP condensates that likely help coordinate multi-step reactions in RNA processing[3].

383 DEAD box RNA helicases appear to be important players in biomolecular condensates[40,45], and we
384 observed three enriched in BR-bodies. We observed that RhlE and DEAD act as scaffolds that undergo
385 RNA-dependent phase separation *in vitro*, while RhlB cannot phase separate alone, but can enter the
386 BR-body through RNase E's IDR, similar to what was observed for their *E. coli* homologues[40], suggesting
387 phase separation is a conserved feature of these helicases. Interestingly, we observed strong
388 recruitment of RhlE and RhlB into RNase E condensates, but DEAD was observed to be recruited to a
389 lower extent (Fig 4). While RhlB was strongly colocalized with RNase E[4] and RhlB foci dissociated in cells
390 after RNase E depletion, RhlE showed heterogenous, partially overlapping localization with RNase E and
391 remained localized in foci even after RNase E depletion (Fig 2). The function of DEAD box proteins in BR-
392 bodies is not well understood; however, RhlE becomes more highly expressed when *C. crescentus* is
393 grown in the cold[35], which may alter the composition and function of BR-bodies in these conditions.

394 BR-body proteomics identified Hfq as a BR-body enriched protein. Hfq chaperones small RNAs to
395 their target mRNAs and represses translation/induces decay[46–50]. It is unsurprising that Hfq was
396 enriched in BR-bodies because the BR-body transcriptome is highly enriched with poorly translated
397 mRNAs and small RNAs[29]. Hfq phase separates with RNA *in vitro* and forms heterogenous colocalized foci
398 in *C. crescentus*. *E. coli* Hfq was recently found to phase separate with DNA, polyphosphate[41], and
399 RNA[10], and its condensation is promoted *in vitro* by its intrinsically disordered CTD[41]. *E. coli* Hfq foci
400 were previously identified to colocalize with RNase E in nitrogen starved *E. coli* cells[7], and, while Hfq is
401 not a core member of the *E. coli* or *C. crescentus* RNA degradosome, it has been found to associate with
402 RNase E in multiple species[51]. Interestingly, we observed that *C. crescentus* Hfq is readily recruited into
403 RNase E-RNA condensates, but RNase E was not recruited into Hfq-RNA condensates, suggesting a
404 preferred directionality in forming a mixed condensate. *E. coli* Hfq condensates promote sRNA-mRNA
405 annealing[10] and RNase E IDR mutants prevent sRNA-mRNA silencing[52]. These RNase E IDR mutants were
406 later found to prevent BR-body phase separation [4] Therefore, the coordination of Hfq with BR-bodies
407 likely helps degrade translationally repressed mRNAs; the same function has been proposed for
408 miRNA/siRNA/LSM in P-bodies[22].

409 The BR-body associated proteins identified that can dissolve BR-bodies, ribosomal protein S1 and
410 MetK, may play important regulatory roles in controlling BR-body assembly. Ribosomal protein S1
411 appears to dissolve RNase E condensates via its RNA binding capacity, while MetK appears to dissolve
412 RNase E via protein-protein interaction with RNase E (Fig 5). Ribosomal protein S1 is present in a
413 ribosome-bound and a ribosome free form; it unfolds structured mRNAs in preparation for translation
414 initiation[53] and protect mRNAs from RNase E-dependent decay[54]. Since BR-bodies and ribosomes
415 compete for mRNA substrates[4], ribosomal protein S1 may prevent BR-body condensation on highly
416 translated mRNAs by locally disrupting RNase E condensation when in polysomes. Alternatively, if
417 ribosomal protein S1 dissociates from the ribosome, it may be able to globally dissolve BR-bodies,
418 potentially acting as a sensor of translation. We found that MetK, an essential enzyme that generates S-
419 adenosylmethionine, could phase separate with RNA. MetK was previously found to bind RNase E in
420 cells grown in the cold [35], and we identified a protein-protein interaction between RNase E and MetK
421 under standard growth temperature (Fig 5, Fig S5C), suggesting MetK likely inhibits RNase E
422 condensation directly by blocking multivalent interactions with RNase E or indirectly by altering the

423 conformation of RNase E. Despite its rather weak RNA binding observed *in vitro*, *C. crescentus* MetK
424 phase separated in the presence of RNA, and homologs from *S. meliloti* and *E. coli* were identified to
425 bind RNA[55]. Because MetK is the sole enzyme creating S-adenosylmethionine in *C. crescentus*, perhaps it
426 might act as a metabolic sensor that could tune the number of BR-bodies to carbon availability. In line
427 with this hypothesis, MetK protein levels are dramatically altered upon carbon starvation[56].

428 **RNA is critically important to BR-body condensation**

429 Excitingly, reconstitution of minimal BR-body cores revealed that RNA, which was hypothesized
430 to play a key role in BR-body assembly *in vivo*[4], plays a key role in BR-body assembly *in vitro*. We
431 observed that RNA can kinetically stimulate the rate of BR-body condensation on the sub-minute
432 timescale (Fig 7), further suggesting that the main cause of RNase E's robust foci dissolution under
433 rifampicin treatment is the RNA depletion induced by rifampicin and not other cellular perturbations
434 from this drug, such as nucleoid expansion[57]. The addition of RNA degradosome proteins does not alter
435 the rate of RNase E condensation, but it does appear to enhance RNase E mobility by FRAP (Fig 7). *In*
436 *vivo*, the RNA present in BR-bodies is likely mostly long, poorly translated mRNAs and small RNAs; BR-
437 bodies are depleted of rRNA and other highly structured ncRNAs[29]. This suggests that, at least under
438 logarithmic growth conditions, the availability of poorly translated RNA helps catalyze rapid BR-body
439 assembly. Interestingly, BR-bodies could be induced with some client proteins in the absence of RNA,
440 such as PNPase; however, the rate of the condensation was far slower than in the presence of RNA.
441 While likely not relevant under log phase growth conditions as BR-bodies were observed to have sub-
442 minute dynamics[4], such assemblies might occur under non-growing conditions, like stationary phase.

443 The identification of five new RNP condensates associated with BR-bodies suggests these
444 structures likely have a broader role in bacterial cell organization than previously anticipated. Indeed,
445 recent high-throughput methods designed to detect proteins crosslinked to RNA identified >1100 RNA
446 binding proteins in *E. coli*, including many metabolic enzymes[58,59]. Similarly, we identified two metabolic
447 enzymes, MetK and FabG, that have the capacity to phase separate with RNA (Fig 3). While the ability of
448 metabolic enzymes to bind to RNA is referred to as "moonlighting" RNA binding activity[60], it is possible
449 that due to the large number of RNA binders, RNP condensates play a broad role in organizing metabolic
450 pathways in the bacterial cytoplasm. Because experimentation to identify and characterize new
451 condensates is a slow process, bioinformatic prediction of proteins that can undergo phase separation is
452 the only method that can be utilized across whole proteomes. However, the current algorithms[61,62] do
453 not accurately predict the phase separation of all five of the proteins we identified. Perhaps current
454 phase separation prediction algorithms rely too much on IDR predictions, which often affect phase
455 separation, but are not always required[63]. When developing next generation algorithms to predict
456 phase separation, it will be important for the training data sets to include bacterial phase separating
457 proteins to improve their predictive power.

458 **Materials and Methods**

459 ***Caulobacter crescentus* cell growth**

460 All *C. crescentus* strains used in this study were derived from the wild-type strain NA1000[64] and were
461 grown at 28°C in peptone-yeast extract (PYE) medium or M2 minimal medium supplemented with 0.2%
462 D-glucose (M2G)[65]. When appropriate, the indicated concentration of vanillate (0.5 mM), xylose (0.2%),
463 gentamycin (Gent) (0.5 mg/mL), kanamycin (Kan) (5 mg/mL), spectinomycin (Spec) (25 mg/mL), and/or

464 streptomycin (Strp) (5 mg/mL) was added. Strains were analyzed at mid-exponential phase of growth
465 (OD 0.3-0.6). Optical density was measured at 600 nm in a cuvette using a Nanodrop 2000C
466 spectrophotometer.

467 **BR-body enrichment assay and LC-MS proteomics**

468 BR-body enrichment was performed as in[30]. Enriched BR-bodies were then resuspended in buffered SDS
469 before proteomics sample preparation.

470 *Suspension Trapping (S-Trap) Sample Preparation:*

471 100 µg protein lysate (JS221 or JS299) was prepared in triplicate according to the manufacturer's
472 instructions. Trypsin was resuspended in a 50 mM ABC buffer and added to S-Traps at a 1:50
473 (enzyme:protein w/w) ratio and incubated for 8 hours at 37˚C. After the digestion, peptides were eluted
474 according to the manufacturer's protocol and vacuum centrifuged to dryness prior to desalting.

475 *Solid Phase Extraction (SPE):*

476 All samples were desalted prior to MS analysis with 10mg HLB cartridges according to manufacturer's
477 instructions as in [66]. Samples were dried prior to analysis and stored at -80˚C until re-suspension for LC-
478 MS.

479 *Analysis via Nano UHPLC-MS/MS:*

480 Dried digests were resuspended in 0.1% formic acid in water to a concentration of 250 ng/µL. 2 µL of
481 solution was injected onto a 100mm x 100µm C_{18} BEH reverse phase chromatography column with an
482 autosampler (nanoACQUITY, Waters Corporation). Peptides were separated over a 95 minute
483 segmented gradient from 4-35% B (A= H_2O + 0.1% FA, B=acetonitrile + 0.1% FA). MS-MS/MS was
484 performed on a Q-Exactive HF mass spectrometer via electrospray ionization (Thermo Fisher Scientific).
485 Samples were collected in biological triplicate, and data were acquired in technical triplicate injections
486 using a TOP17 data-dependent method (DDA).

487 *Peptide-Spectrum Matching (PSM):*

488 RAW files from technical and biological triplicates were processed for peptide identification, protein
489 inference, and false-discovery rate using the MetaMorpheus search engine[67]. A *C. crescentus* FASTA
490 from UniProt (proteome ID UP000001364) was used with a common contaminant file. Data were first
491 calibrated prior to search ('Traditional') using the default parameters. For 'Main' search, additional
492 parameters included a maximum of two missed cleavages, two variable modifications per peptide, and a
493 minimum peptide length of seven amino acids. The precursor mass tolerance was set to 5 ppm and the
494 product mass tolerance was set to 20 ppm. The 'common' fixed and 'common' variable modifications
495 were selected, and identifications were filtered to a q-value of <0.01. RAW data files are available
496 through MassIVE with accession number (MSV000090894).

497 ***In vivo* localization of BR-body associated proteins**

498 All *C. crescentus* protein fusion strains were grown in PYE-Kan or PYE-Gent media overnight. The next
499 day, from the mid log-phase cultures, serial dilutions were done in M2G medium containing the
500 appropriate amount of Kan or Gent and cells were grown overnight. The next day, the mid log-phase
501 cultures were induced with 0.5 mM vanillate and grown for 6 hours. 1µL of the cells were spotted on a

502 M2G 1.5% agarose pad, a cover slip was added, immersion oil was spotted on the cover slip, and the
503 cells were imaged using a YFP filter cube.

504 **RNase E depletion**

505 Depletion strains containing the xylose-inducible copy of RNase E were first grown overnight in M2G-
506 Kan-Gent medium containing 0.2% xylose. The next day, from the log-phase cultures, serial dilutions
507 were prepared in M2G-Kan-Gent medium containing 0.2% xylose overnight. Mid-log phase cells were
508 then washed 3 times with 1 mL growth medium, resuspended in growth medium, and split equally into
509 two tubes. 0.2% xylose was added to one tube. Depletion strains were analyzed at the mid-exponential
510 phase of growth (OD 0.3-0.6) and after 24 hours of depletion of xylose. 1 µL of the cells under each
511 condition were spotted on a M2G 1.5% agarose pad, a cover slip was added, immersion oil was spotted
512 on the cover slip, and the cells were imaged using a YFP filter cube.

513 **Colocalization of YFP tagged foci forming proteins with BR-body markers**

514 Dual-labeled strains expressing foci-forming proteins in Fig 2A with BR-body markers RNase E or
515 Aconitase were first grown in PYE medium containing the appropriate amount of Kan, Gent, Spec or Strp
516 overnight. The next day, from log-phase cultures, serial dilutions were done in M2G medium. The
517 following day, mid log-phase cells were split into two tubes, and one was treated with an inducer (0.5
518 mM vanillate or 0.02% xylose), and both were grown for 6 hours. 1 µL of the cells under each condition
519 was spotted on a M2G 1.5% agarose pad, a cover slip was added, immersion oil was spotted on the
520 cover slip, and the cells were imaged using YFP, CFP, GFP, and TX-Red filter cubes. A dual-labeled strain
521 expressing PopZ-mCherry with RNase E-GFP was used as a negative control. Fluorescence level analysis
522 of the droplets was performed using MicrobeJ[68]. Line traces were performed using ImageJ and the
523 correlation analysis between channels was performed in Microsoft Excel.

524 ***In vivo* localization of RNase E-GFP foci in the strains with BR-body enriched proteins deleted**

525 JS671, JS672, JS735, and JS744 strains were grown in PYE medium containing the appropriate amount of
526 Kan, Gent, Spec or Strp overnight. The next day, from the log-phase cultures, serial dilutions were done
527 in M2G medium overnight. The following day, 1µL of the mid-log cells were spotted on a M2G 1.5%
528 agarose pad, a cover slip was added, immersion oil was spotted on the cover slip, and the cells were
529 imaged using a GFP filter cube.

530 **Dissolution of MetK and ribosomal protein S1**

531 Strains expressing MetK and ribosomal protein S1 with BR-body marker Aconitase-mCherry were first
532 grown overnight in PYE-Kan-Spec-Strp medium in 3 serial dilutions. Mid log-phase cells were split
533 equally into two tubes, one was treated with 0.2% xylose, and the cells were grown for 6 hours. 1 µL of
534 the cells under each condition was spotted on a M2G 1.5% agarose pad and imaged using TX-Red filter
535 cubes.

536 **Cell imaging**

537 Around 1 µL of cells were immobilized on 1.5% agarose pads made with M2G medium on microscope
538 slides (Thermo Fisher Scientific 3051). Cell droplets were allowed to air dry, were covered by a cover
539 slip, and imaged with immersion oil. All images were collected using a Nikon Eclipse NI-E with CoolSNAP
540 MYO-CCD camera and 100x Oil CFI Plan Fluor (Nikon) objective, driven by Nikon elements software. The

541 filter sets used for YFP, CFP, GFP, and mCherry imaging were chroma 96363, 96361, 96362, and 96322
542 models respectively. Cell image analysis was performed using MicrobeJ[68].

543 **RNA extraction**

544 For RNA extraction, mid-log phase cells (0.3 to 0.5 OD600) were pelleted at 20,000 g for 10 minutes in a
545 microcentrifuge. Then, the cells were resuspended in 1mL 65°C Trizol (1mL for each 1 mL of NA1000
546 cells) and incubated at 65°C for 10 min in a heat block. 200 µL of chloroform was added and incubated
547 for 5 min at room temperature. The samples were then spun at max speed (20,000 g) in a
548 microcentrifuge for 10 min at room temperature. The aqueous layer was removed and RNA samples
549 were precipitated using 700 µL isopropanol at -80°C for 1 hour and spun at 20,000 g for 1 hour at 4°C.
550 The supernatant was removed and the pellet was washed with 1 mL of 70% ethanol. The samples were
551 then spun again for 10 min at 20,000 g at 4°C, the supernatant was removed, and the pellet was
552 resuspended in RNase-free water. RNA samples were run on 1X TBE/7M urea denaturing PAGE gels and
553 visualized with SYBR Gold nucleic acid gel stain.

554 **Protein purifications**

555 The protein coding genes were cloned into pET His6 MBP TEV,pET His6 G TEV, or pET28a plasmids and
556 the expressed proteins were purified by His tag affinity purification, followed by the removal of the MBP
557 or G tag by TEV proteolysis. RNase E CTD, RhlB, RhlE-IDR were expressed as N-terminal MBP fusions and
558 all the other proteins were expressed as N-terminal G protein fusions. Briefly, the proteins were
559 expressed in BL21 DE3 cells by inducing with 0.5mM IPTG at 37° C for 3.5 hours in 2X Luria-Bertani
560 medium. The cells were then pelleted at 5000 rpm for 20 minutes and were lysed in a lysis buffer
561 (20mM Tris pH 7.4, 500mM NaCl, 10% glycerol, 10mM imidazole, 1mM PMSF, 1 tablet protease inhibitor
562 cocktail, and DNase I) at 4° C using a sonicator with 10 seconds pulse on and 30 seconds pulse off times
563 for 18 cycles. The lysed cells were centrifuged at 15,000 rpm for 45 minutes and the resultant
564 supernatant was loaded onto equilibrated Ni-NTA resin, the protein-bound resin was washed with 10
565 column volumes each of lysis buffer, chaperone buffer (20 mM Tris pH 7.4, 1 M NaCl, 10% glycerol, 10
566 mM imidazole, 5 mM KCl, 10 mM MgCl2, and 2 mM ATP), and low salt buffer (20 mM Tris pH 7.4, 1 M
567 NaCl, 10% glycerol, and 10 mM imidazole). The proteins were eluted in elution buffer (20 mM Tris pH
568 7.4, 150 mM NaCl, 10% glycerol, and 250 mM imidazole) and dialyzed into storage buffer (20 mM Tris
569 pH 7.4, 150 mM NaCl). The contaminant proteins were removed by passing through a S200 size
570 exclusion column. The concentrated proteins were stored at -80°C.

571 RNase E CTD purification: His6-MBP-TEV-RNase E CTD was expressed and purified in the same way as
572 described above except the lysis buffer additionally contained 1M NaCl and 0.1% Triton X-100.

573 Hfq purification: Hfq protein was expressed at 18°C for 16 hours. The lysis buffer and elution buffer
574 contained 1 M NaCl instead of 150 mM and 500 mM NaCl, respectively. To remove the contaminating
575 nucleic acids, the His tag affinity purified protein was treated with 30 µg/mL RNase A and 5 U/mL DNase
576 I for 1 hour at 37° C, concentrated, and loaded onto a HiLoad 16/60 Superdex 200 size exclusion column
577 (GE healthcare). The absence of RNase A was further validated by incubating RNA with the protein.

578 **Cyanine 5 Protein labeling**

579 Labeling reactions were carried out according to the manufacturer's protocol (Lumiprobe). Cy5 NHS
580 ester dye dissolved in DMSO was incubated with proteins at an equal ratio in 0.1M sodium bicarbonate

581 buffer pH 8.5 at room temperature for 4 hours. A protein labeling calculator
582 (https://www.lumiprobe.com/calc/protein-labeling) was used to calculate the amount of protein and
583 dye used in the labeling reactions. The excess dye was removed by dialyzing against protein storage
584 buffer (20mM Tris pH 7.4, 150mM NaCl) using a 3 kDa cut off dialysis cassette. Degree of labeling was
585 calculated using the formula:

$$number\ of\ Cy5\ dye\ per\ protein = \frac{molarity\ of\ Cy5\ dye}{molarity\ of\ protein}$$

$$[molarity\ of\ Cy5\ dye] = \frac{A650}{650}$$

$$molarity\ of\ protein = \frac{A280c}{280}$$

$$A650 = conjugate\ absorbance\ at\ 650nm$$

$$650 = molar\ extinction\ coefficient\ of\ Cy5\ dye$$

$$A280c = conjugate\ corrected\ absorbance\ at\ 280nm = A280 - \left(A650 * (0.05)\right)$$

$$280 = molar\ extinction\ coefficient\ of\ protein$$

586 ***In vitro* phase separation experiments and droplet assays**

587 Proteins were incubated at their *in vivo* concentrations in the presence or absence of *C. crescentus* total
588 RNA (20 ng/µL) in 20mM Tris pH 7.4, 100mM NaCl for 30 minutes at room temperature. The mixture
589 was pipetted onto a glass slide, covered with a cover slip, and imaged using a Nikon epifluorescence
590 microscope. For quantification of the number and distribution of droplets, 10 images for each protein
591 were analyzed using the "analyze particles" function in ImageJ..

592 For the recruitment assays, 6 µM RNAse E CTD was incubated with 20 ng/µL of *C. crescentus* total RNA in
593 20mM Tris pH 7.4, 100mM NaCl for 20 minutes at room temperature, followed by the addition of Cy5-
594 labeled client proteins and an additional incubation for 20 minutes before imaging. The level of
595 recruitment was assessed by calculating the partition coefficient of client proteins. 30 droplets were
596 analyzed in each case.

$$partition\ coefficient = \frac{mean\ fluorescence\ intensity\ inside\ the\ droplets}{mean\ fluorescence\ intensity\ outside\ the\ droplets}$$

597 ImageJ software was used to quantify the mean fluorescence and the data were plotted in
598 PlotsOfData[69]. Co-assembly experiments were performed by mixing all the components and incubating
599 for 30 minutes at room temperature before imaging.

600 For the salt and RNA dependency experiments, preformed protein and RNA condensates were
601 incubated with either varying concentrations of NaCl or RNase A for 30 minutes at room temperature
602 before the solution was imaged on a glass slide using phase contrast microscopy.

603 RNase E condensation induction in the absence of RNA was carried out by adding client proteins at
604 varied concentrations to 6 µM RNase E CTD in 20mM Tris, 100mM NaCl and incubating for 30 minutes at
605 room temperature. The solution was imaged on a glass slide using phase contrast microscopy.

606 ***In-vitro* protein pull down assay**

607 The RNAse E CTD tagged with maltose binding protein (MBP) or MBP only was incubated with bait
608 proteins in pull down binding buffer (20mM HEPES pH 7.4, 100mM NaCl, 2% glycerol, and 2mM DTT) for
609 60 minutes at room temperature. 100 µL of dextrin agarose resin was added to the above mixture and
610 incubated for another 90 minutes at 4°C on a tube rotator. The samples were washed four times with 1
611 mL of wash buffer (20mM HEPES pH 7.4, 100mM NaCl). Bound proteins were eluted with 100 µL of
612 elution buffer (20mM HEPES pH 7.4, 150mM NaCl, 10mM maltose) at 30ºC with constant shaking. The
613 eluted proteins were resolved on an SDS PAGE gel.

614 **Electrophoretic mobility shift assay**

615 RNA (50 nM) was incubated with the specified concentrations of proteins for 30 minutes at room
616 temperature in binding buffer (20mM Tris pH 7.4, 150mM NaCl, 5% glycerol, 2mM DTT, 1mM EDTA, and
617 10 µg/mL BSA). The incubated samples were resolved on a 5% acrylamide/bis-acrylamide native gel
618 (prepared in TBE buffer) at 4°C in 0.5X TBE running buffer. The gel was stained with SYBR Gold for 20
619 minutes and scanned using a Typhoon scanner.

620 **Bacterial Two-Hybrid assay**

621 The bacterial two-hybrid assay was carried out as described previously in[42]. The bait protein RNase E was
622 cloned into the pKNT25 plasmid (kanamycin resistance) using Xba1 and EcoR1 sites and the prey protein
623 MetK was cloned into the pUT18 plasmid (ampicillin resistance) using Xba1 and Sac1 sites. The sequence
624 verified plasmids were transformed into chemically competent BTH101 cells (adenylate cyclase
625 deficient) and the colonies were selected on LB-agar plates containing kanamycin (50 µg/mL), ampicillin
626 (100 µg/mL), X-gal (40 µg/mL), and IPTG (0.5mM), and incubated at 30°C for 72 hours. The resultant
627 blue colonies were grown in LB-medium containing kanamycin (30 µg/mL) and ampicillin (50 µg/mL) and
628 log phase cells were plated onto LB-agar plates containing kanamycin, ampicillin, X-gal, and IPTG as
629 mentioned above. The positive control cells were transformed with pKNT25-Zip and pUT18-Zip plasmids,
630 which upon expression reconstitute a functional adenylate cyclase enzyme. The negative control cells
631 were transformed with the pKNT25 and pUT18 plasmids.

632 **Determination of the assembly order of RhlE, RNase E, and Aconitase foci**

633 *C. crescentus* JS716 (RhlE-YFP/Aconitase-mCherry) and JS452 (RNase E-YFP/Aconitase-mCherry) were
634 grown overnight in PYE medium containing kanamycin (5 µg/mL), spectomycin (25 µg/mL), and
635 streptomycin (5 µg/mL) until the cultures reached mid log-phase (OD ~0.3). Prior to imaging, the cells
636 were diluted to 0.05 OD in PYE media and induced with 0.02% xylose for 15 minutes at 28°C. Aliquots of
637 1.5 µL of culture were spotted onto pads of 2% agarose in M2G medium and sandwiched between two
638 coverslips. Cells were imaged with an Olympus IX71 inverted epifluorescence microscope with a 100×
639 objective (NA 1.40, oil immersion) kept at 28 °C using an objective heater (Bioptechs). The YFP fusion
640 proteins were imaged under excitation from a 488-nm laser (Coherent Cube 488-50; 0.4 W cm^{-2}) and the
641 mCherry fusions were imaged under excitation from a 561-nm laser (Coherent Sapphire 561-50; 2.0 W
642 cm^{-2}). Both channels were imaged simultaneously on a 512 × 512 pixel Photometric Evolve electron-

643 multiplying charge-coupled device (EMCCD) camera, using an OptoSplit II image splitter (Cairn Research)
644 with a 635-nm long pass filter and a 525/50 nm bandpass filter. An integration time of 250 ms with a
645 delay between frames of 5 s was used, where a shutter blocked irradiation during the delay time to
646 minimize photobleaching of YFP and mCherry.

647 To analyze the fluorescence intensities, the mean intensity of each cell in each channel was first
648 subtracted from the movies. Foci were then detected by eye in the background-subtracted movies, and
649 the mean and maximum intensities within the 9 × 9 pixel region of interest (ROI) surrounding each focus
650 was measured in both channels. Time zero was set to be the frame immediately preceding the first
651 frame with an ROI mean intensity at least 10% higher than the maximum intensity value in the ROI in
652 the previous frame. This time zero was also assigned as time zero on the other channel. Subsequently,
653 the maximum intensity within the ROI was divided by the maximum intensity of the ROI in the time zero
654 frame to determine the fluorescence intensity enhancement of each focus at each time.

655 **Condensate growth kinetic assays**

656 Time lapse images were acquired using a Zeiss LSM 800 microscope. 6 µM of RNase E CTD YFP (RCY) was
657 spotted onto a glass slide, and either RNA or proteins or both at the specified concentrations were
658 pipetted onto the RCY solution. Image acquisition was started before the addition of RNA or proteins or
659 both, but the zero minute time point was calculated from the time they were added to the RCY solution
660 on the glass slide. The zero minute time point for 'RCY only' started from the time the sample was
661 spotted onto the glass slide. The images were acquired for 2.5 minutes with a 50 ms time interval. The
662 data were quantified in ImageJ and plotted in MS Excel.

663 **QUANTIFICATION AND STATISTICAL ANALYSIS**

664 **Foci quantification**

665 *In vivo* protein fusion foci were quantified using MicrobeJ[68]. Cell outlines were first identified using the
666 medial axis algorithm in the phase channel with a minimal cell length of 1.35 µm and the segmentation
667 option. Cell outlines were then manually curated to remove cells containing erroneous outlines. Next,
668 the maxima function was used with the ''foci'' option with a minimal area of 0.01 μm^2 and minimal
669 length of 0.1 µm with the segmentation option on and the association inside option on. Tolerance and Z-
670 score parameters were tuned for each protein fusion type.

671 To quantify the average foci per cell of each strain, three replicates were performed on three different
672 days and three images were analyzed from each day. We summed all foci identified in each cell and
673 divided by the total number of cells to calculate number of foci per cell.

674 **Colocalization analysis**

675 Dual channel images of enriched BR-body protein fusions with BR-body markers were analyzed via the
676 line trace method to assess colocalization. For each focus identified, we drew a line through the focus
677 and quantified the intensity vector across the line. We then analyzed the other channel across the same
678 line, and calculated the correlation of the intensity of each channel. The images were analyzed for a
679 minimum of 30 foci identified in the BR-body enriched protein (presented in Fig 2B). PopZ-mCherry was
680 used as a negative control for the analysis.

681 **FRAP assays**

682 FRAP was performed according to a standard protocol [70]. Briefly, the measured F(t) over the bleached
683 circular area of diameter (d) = 2 µm, normalized by that of the unbleached region of the same diameter,
684 F(0), was fitted by a one-phase exponential function using the "Bottom to (Span+ Bottom)" analysis as
685 $F(t)/F(0) = Bottom + Span*(1 - \exp(-t \ln 2/\tau_{1/2}))$, where $\tau_{1/2}$ is the halftime for diffusion. The apparent
686 diffusion coefficient, D, was obtained from $\tau_{1/2}$ according to $D = d2/(4\tau_{1/2})$.

687 Figure Legends

688 **Figure 1.** BR-body enrichment proteomics identifies BR-body associated proteins. A) *Caulobacter*
689 *crescentus* BR-body enrichment[30] was performed, followed by LC-MS/MS proteomics to identify BR-body
690 associated proteins. JS299 (an RNase E active site mutant) was used to isolate BR-bodies, and JS221 (an
691 RNase E mutant lacking the C-terminal disordered region that cannot form BR-bodies) was used as a
692 negative control. B) BR-body enrichment analysis from the LC-MS/MS proteomics data. The RNA
693 degradosome proteins were identified by pulldown from[31,34,35]. Polar proteins were identified as
694 interactors with PopZ[38] or polar condensates with interactions with PopZ, PodJ, or SpmX. Polar proteins
695 measured in the negative control but undetected in the BR-body enriched samples were plotted at <-5.
696 T-tests with uneven variance were used for statistical comparison. GO-term enrichment for localization
697 and protein function were performed using NCBI DAVID[71].

698 **Figure 2.** RNase E is required for the foci formation and BR-body colocalization of most BR-body
699 associated proteins. A) The localization pattern of foci-forming YFP fusions. All genes were placed under
700 control of the vanillate promoter and grown in M2G minimal media. *In vivo* protein fusion strains were
701 analyzed at mid-exponential phase of growth (OD 0.3-0.6) following 6-hours of induction with 0.5mM
702 vanillate. and quantified using MicrobeJ[68]. Three replicates were performed on three different days and
703 three images were analyzed from each day to calculate the average number of foci per cell. A minimum
704 of 150 cells were used for each YFP-fusion for the analysis. Error bars represent the standard error.
705 Representative images are in supplementary figure 1 (Fig S1). B) Colocalization patterns of the BR-body
706 enriched protein fusions with BR-body markers. Colored line traces indicate the pattern of localization
707 observed for individual foci. The line trace method was used to assess enrichment. The correlation was
708 calculated for each line trace using the BR-body enriched protein (client) as a reference, and each line
709 trace correlation value was plotted as a single dot on the plot. A minimum of 30 foci for each BR-body
710 enriched protein were used for the analysis. The median value is represented as a black line. Statistics
711 were based upon a two-tailed t-test with unequal variance. C) Subcellular localization patterns of *C.*
712 *crescentus* protein-YFP strains expressed from the *vanA* locus in the RNase E depletion background
713 where the sole copy of the RNase E gene is controlled by the xylose promoter. The YFP intensity of
714 Aconitase-YFP was too low to measure when expressed from the vanillate promoter, so a native gene
715 fusion was used instead. The YFP intensity of each image was normalized from its brightest level relative
716 to its background level. Depletion strains were analyzed at mid-exponential phase of growth (OD 0.3-
717 0.6) and after 24 hours of xylose depletion. Quantitation of the number of *Ccr* protein-YFP foci per cell
718 measured in M2G minimal media with xylose (+Xyl) and M2G minimal media lacking xylose (-Xyl) for the
719 same strains in Fig S2. The squares represent the strains whose levels were too low to detect. All images
720 were quantified using MicrobeJ[68]. Three replicates were performed on three different days and three
721 images were analyzed from each day to calculate the average number of foci per cell. A minimum of 175
722 cells were used for the analysis. Error bars represent the standard error. Representative images in
723 supplementary figure 2(Fig S2). Foci/cell calculations were performed as in A. D) RNase E GFP foci per
724 cell were measured in wild type, rhlB, rhlE, and hfq mutant backgrounds. Foci/cell calculations were

725 performed as in A. Error bars represent the standard error from a minimum of 100 cells. Scale bar is 1
726 μm for all images.

727 **Figure 3**. Some BR-body enriched proteins can drive RNA-dependent biomolecular condensation. A)
728 (Left) Domain organization of proteins that undergo LLPS. The red line indicates disordered regions as
729 predicted by PONDR. (Right) Prediction of the propensity to LLPS by Disorderness[72], Pscore[67],
730 Catgranule[73] and DeePhase[62] scores. B) Phase contrast microscopy images of the purified proteins
731 incubated at their *in vivo* concentrations (DEAD (5 μM), Hfq (5 μM), RhlE (2 μM), FabG (5 μM), MetK (10
732 μM)) in standard buffer (20mM Tris pH 7.4, 100mM NaCl, 1mM DTT) in the presence and absence of *C.*
733 *crescentus* total RNA (200 ng). Scale bar is 3μm for all images. C) Droplets are dissolved by NaCl and
734 RNase A. The dissolution of droplets was tested by adding either 0.5M NaCl or RNase A (1 μg) to the
735 preformed droplets. All of the proteins were found to be NaCl and RNase sensitive.

736 **Figure 4.** Many BR-body associated proteins are directly recruited to RNase E condensates *in vitro.* A)
737 Cartoon showing the *in vitro* RNase E droplet recruitment assay. Cy5 labeled proteins are added to
738 preformed RNase E CTD+RNA droplets. Microscopy images of the droplets are taken in phase contrast
739 and Cy5 fluorescence, and the partition coefficient of the fluorescence signal is calculated for each
740 droplet. B) Partition coefficient (PC) of Cy5 labeled client proteins in RNase E CTD (6 μM) + total RNA
741 (200ng) droplets. Negative controls BSA-Cy5 and SpmX-Cy5 have partition coefficients of 1. The black
742 horizontal line through the plot indicates a PC of 1, which is the "no enrichment" baseline. PC of
743 ribosomal protein S1 and MetK proteins could not be determined because of the dissolution of droplets.
744 The data were quantified in ImageJ software and plotted in PlotsofData[69]. For the example images
745 presented, the left image is phase contrast and the right image is the Cy5 channel of each indicated
746 protein. The scale is 10 μm for all images. Concentrations of proteins used to quantify the partition
747 coefficient: PNPase (5 μM), Aconitase (5 μM), RhlB (4 μM), RND (5 μM), DEAD(5 μM), Hfq (5 μM), DnaK
748 (5 μM), FabG (5 μM), NudC (2.5 μM), RppH (1 μM), Rho (5 μM), NusG (5 μM), TyrRS (5 μM), and SpmX (5
749 μM). BSA was added at a 5 μM concentration.

750 **Figure 5.** Ribosomal protein S1 and MetK dissolve BR-bodies *in vitro* and *in vivo.* A) Microscopy images of
751 *in vitro* RNase E droplets incubated with either ribosomal protein S1 or MetK. RNA-induced RNase E
752 droplets are shown at the top and PNPase-induced RNase E droplets are shown below. The scale is 10
753 μm for all images. Concentrations used were: RNase E CTD (10 μM), S1 (5 μM), MetK (5 μM), PNPase (5
754 μM), and total RNA (20ng/μL). B) RNA and protein binding data for ribosomal protein S1 and MetK with
755 1 μM RNA. RNA was visualized by SYBR Gold staining. C) Aconitase and MetK pull-down with RNase E. 5
756 μM RNase E CTD MBP or MBP were incubated with 5 μM of Aconitase or 15 μM of MetK or 15 μM of S1
757 protein. Eluates were resolved on 10% SDS PAGE. Aconitase and MetK pulled down with RNase E CTD
758 MBP, while S1 protein did not. None of the proteins pulled down with MBP alone. D) Bacterial 2 hybrid
759 assay plate showing the spots of BTH101 cells cotransformed with plasmids expressing the proteins as
760 indicated in the figure. Blue colored spots represent an interaction between the two proteins. The pairs
761 RNase E-T25/Aconitase-T18, RNase E-T25/MetK-T18 and positive control pair T25-Zip/T18-Zip showed
762 interactions and the other pairs showed no interaction. Underneath is a proposed cartoon of the RNA
763 dependence of droplet dissolution by S1 and MetK. E) BR-bodies (marked with Aconitase-mCherry) are
764 dissolved upon overexpression of ribosomal protein S1 or MetK from the pBX multicopy plasmid.
765 Quantitation of the average Aconitase-mCherry foci per cell was performed using MicrobeJ and is
766 plotted on the right (error bars represent the standard error). A minimum of 700 cells were used for
767 each analysis.

768 **Figure 6.** BR-body associated drivers have distinct condensation and client recruitment profiles. A)
769 Scaffold proteins recruit a distinct subset of client proteins. Each RNA degradosome client, labeled with
770 Cy5, was tested for recruitment into pre-formed condensates of each BR-body associated scaffold
771 indicated on the left. BR-body associated scaffolds drive a complex network of dependencies controlling
772 phase separation. Each protein scaffold was incubated with RNA and allowed to phase separate. Then a
773 small concentration of Cy5 labeled proteins were tested for entry into the condensate by measuring the
774 partition coefficients of the Cy5 channel. The partition coefficient was calculated from at least 50
775 droplets in each case. The data was quantified in ImageJ. Concentrations of the scaffolds used for
776 making condensates were: RNase E (6 μM), RhlE (5 μM), DEAD (5 μM), Hfq (5 μM), and FabG (10μM).
777 Concentrations of the labeled clients added were: RhlB (4 μM), PNP (5 μM), Aconitase (5 μM), and RND
778 (5 μM). B) BR-body associated scaffolds drive a complex network of dependencies controlling phase
779 separation. Each protein scaffold was incubated with RNA and allowed to phase separate. Then a small
780 concentration of Cy5-labeled proteins was tested for entry into the condensate by measuring the
781 partition coefficients of the Cy5 channel. Concentrations of the scaffolds used for making condensates
782 were: RNase E (6 μM), RhlE (5 μM), DEAD (5 μM), Hfq (5 μM), and FabG (10 μM). Concentrations of the
783 labeled scaffolds added were: RNase E (1 μM), RhlE (0.5 μM), DEAD (1 μM), Hfq (1 μM), and FabG (1
784 μM). Scaffold proteins recruit a distinct subset of client proteins. Each RNA degradosome client labeled
785 with Cy5 was tested for recruitment into each BR-body associated scaffold. Each dot in (A) and (B) plots
786 indicate the partition coefficient in a single droplet. The partition coefficient was calculated from at
787 least 50 droplets in each case. The data were quantified in ImageJ. C) Order of assembly experiments
788 using GFP-RNase E (6 μM) and RhlE-Cy5 (5 μM) condensates. "Condensed simultaneously" indicates that
789 both proteins were added together before the addition of RNA (20ng/μL) to trigger condensation.
790 "Condensed separately" indicates that both proteins were incubated with RNA (20ng/μL) yielding
791 separate condensates that were then mixed together. D) *In vivo* order of foci assembly. Time-lapse
792 two-color imaging of RhlE-YFP and Aconitase-mCherry proteins was performed and the evolution of the
793 intensity of each focus after formation is plotted. (i) Intensity evolution in cells in which both Aconitase-
794 mCherry and RhlE-YFP condensates are formed at approximately at the same time. The middle line
795 indicates the average value and the colored region represents the standard deviation between all
796 replicate events. N is the number of events imaged. (ii) Cells in which RhlE-YFP condensates were
797 formed first and the subsequent appearance of Aconitase-mCherry in RhlE-YFP condensates was
798 tracked. (iii) Cells in which Aconitase-mCherry condensates were formed first and the subsequent
799 appearance of RhlE-YFP in Aconitase-mCherry condensates was tracked.

800 **Figure 7.** RNA stimulates rapid BR-body condensation *in vitro*. A) Time lapse imaging of RNase E CTD YFP
801 (RCY) condensate formation. 6 μM RCY assembly was monitored either alone or with different
802 combinations of 100ng/μL RNA, 5 μM PNPase, or all of the degradosome proteins (5 μM PNPase, 4 μM
803 RhlB, 5 μM RNase D1, and 5 μM Aconitase) as indicated on the left. The images were captured at 20X
804 magnification at the time points indicated above. The scale bar is 20 μm. B) Quantification of
805 condensate growth by calculation of the % area occupied in the time lapse experiments from panel A.
806 The data were quantified in ImageJ, averaged from three independent replicates, and plotted in MS
807 Excel. C) Apparent FRAP recovery for droplets with the indicated composition. Because no RCY
808 condensates were present at 6 μM, the concentration was increased to 30 μM to induce condensates.
809 The values are averages from at least six different droplets, and the error bars represent the standard
810 deviation.

Graphical Abstract. Summary of the BR-body protein interactome. Lines between two protein circles represent a direct interaction.

Authors Contribution:

VN performed protein purifications, all *in vitro* experiments, bacterial 2 hybrid assay, and *in vivo* experiments. IWR performed protein purifications, *in vivo* expression, depletion, and colocalization experiments, and made plasmids and strains for *in vivo* experiments. VN, AH, JV performed droplet kinetic assays and FRAP experiments. KM, AG, and YH purified proteins. NM purified BR bodies for BR-body proteomics. CBM and MC performed LC-MS data collection and analysis. LAOR performed RhlE *in vivo* assembly experiments. VN, IWR, and JMS wrote the paper.

Acknowledgements:

NIH grant R35GM124733 to JS. NIH grants R01GM143182 and R01GM144731 to JB. NIH Grant R01GM136863 to WSC. NSF grant CMMI-1914436 to YZ. NIH grant R01GM139277 to MC. We would like to acknowledge the Mass Spectrometry and Proteomics Facility at Notre Dame. *Caulobacter* cell and protein icons in the graphical abstract were created with Biorender.com. The authors thank Vincent Lawal for help with Bacterial 2 hybrid assay. The authors thank Erin Schrader for critical feedback.

References:

1. Azaldegui, C.A., Vecchiarelli, A.G., and Biteen, J.S. (2021). The emergence of phase separation as an organizing principle in bacteria. Biophysical Journal *120*, 1123–1138. 10.1016/j.bpj.2020.09.023.

2. Banani, S.F., Lee, H.O., Hyman, A.A., and Rosen, M.K. (2017). Biomolecular condensates: organizers of cellular biochemistry. Nature Reviews Molecular Cell Biology *18*, 285–298. 10.1038/nrm.2017.7.

3. Nandana, V., and Schrader, J.M. (2021). Roles of liquid–liquid phase separation in bacterial RNA metabolism. Current Opinion in Microbiology *61*, 91–98. 10.1016/j.mib.2021.03.005.

4. Al-Husini, N., Tomares, D.T., Bitar, O., Childers, W.S., and Schrader, J.M. (2018). α-Proteobacterial RNA Degradosomes Assemble Liquid-Liquid Phase-Separated RNP Bodies. Molecular Cell *71*, 1027-1039.e14. 10.1016/j.molcel.2018.08.003.

5. Ladouceur, A.-M., Parmar, B.S., Biedzinski, S., Wall, J., Tope, S.G., Cohn, D., Kim, A., Soubry, N., Reyes-Lamothe, R., and Weber, S.C. (2020). Clusters of bacterial RNA polymerase are biomolecular condensates that assemble through liquid–liquid phase separation. PNAS *117*, 18540–18549. 10.1073/pnas.2005019117.

6. Lasker, K., von Diezmann, L., Zhou, X., Ahrens, D.G., Mann, T.H., Moerner, W.E., and Shapiro, L. (2020). Selective sequestration of signalling proteins in a membraneless organelle reinforces the spatial regulation of asymmetry in Caulobacter crescentus. Nature Microbiology *5*, 418–429. 10.1038/s41564-019-0647-7.

7. McQuail, J., Switzer, A., Burchell, L., and Wigneshweraraj, S. (2020). The RNA-binding protein Hfq assembles into foci-like structures in nitrogen starved Escherichia coli. Journal of Biological Chemistry *295*, 12355–12367. 10.1074/jbc.RA120.014107.

847 8. Monterroso, B., Zorrilla, S., Sobrinos-Sanguino, M., Robles-Ramos, M.A., López-Álvarez, M., Margolin,
848 W., Keating, C.D., and Rivas, G. (2019). Bacterial FtsZ protein forms phase-separated condensates
849 with its nucleoid-associated inhibitor SlmA. EMBO reports *20*, e45946. 10.15252/embr.201845946.

850 9. Wang, H., Yan, X., Aigner, H., Bracher, A., Nguyen, N.D., Hee, W.Y., Long, B.M., Price, G.D., Hartl, F.U.,
851 and Hayer-Hartl, M. (2019). Rubisco condensate formation by CcmM in β-carboxysome biogenesis.
852 Nature *566*, 131–135. 10.1038/s41586-019-0880-5.

853 10. Goldberger, O., Szoke, T., Nussbaum-Shochat, A., and Amster-Choder, O. (2022). Heterotypic
854 phase separation of Hfq is linked to its roles as an RNA chaperone. Cell Reports *41*, 111881.
855 10.1016/j.celrep.2022.111881.

856 11. Feng, Z., Chen, X., Wu, X., and Zhang, M. (2019). Formation of biological condensates via phase
857 separation: Characteristics, analytical methods, and physiological implications. Journal of Biological
858 Chemistry *294*, 14823–14835. 10.1074/jbc.REV119.007895.

859 12. Mittag, T., and Pappu, R.V. (2022). A conceptual framework for understanding phase separation
860 and addressing open questions and challenges. Molecular Cell *82*, 2201–2214.
861 10.1016/j.molcel.2022.05.018.

862 13. Kar, M., Dar, F., Welsh, T.J., Vogel, L.T., Kühnemuth, R., Majumdar, A., Krainer, G., Franzmann,
863 T.M., Alberti, S., Seidel, C.A.M., et al. (2022). Phase-separating RNA-binding proteins form
864 heterogeneous distributions of clusters in subsaturated solutions. Proceedings of the National
865 Academy of Sciences *119*, e2202222119. 10.1073/pnas.2202222119.

866 14. Ditlev, J.A., Case, L.B., and Rosen, M.K. (2018). Who's In and Who's Out—Compositional Control
867 of Biomolecular Condensates. Journal of Molecular Biology *430*, 4666–4684.
868 10.1016/j.jmb.2018.08.003.

869 15. Hubatsch, L., Jawerth, L.M., Love, C., Bauermann, J., Tang, T.D., Bo, S., Hyman, A.A., and Weber,
870 C.A. (2021). Quantitative theory for the diffusive dynamics of liquid condensates. eLife *10*, e68620.
871 10.7554/eLife.68620.

872 16. Taylor, N.O., Wei, M.-T., Stone, H.A., and Brangwynne, C.P. (2019). Quantifying Dynamics in
873 Phase-Separated Condensates Using Fluorescence Recovery after Photobleaching. Biophysical Journal
874 *117*, 1285–1300. 10.1016/j.bpj.2019.08.030.

875 17. Collins, M., Tomares, D.T., Schrader, J.M., and Childers, W.S. (2022). RNase E biomolecular
876 condensates stimulate PNPase activity. 2022.06.06.495039. 10.1101/2022.06.06.495039.

877 18. Peeples, W., and Rosen, M.K. (2021). Mechanistic dissection of increased enzymatic rate in a
878 phase-separated compartment. Nat Chem Biol *17*, 693–702. 10.1038/s41589-021-00801-x.

879 19. Tibble, R.W., Depaix, A., Kowalska, J., Jemielity, J., and Gross, J.D. (2021). Biomolecular
880 condensates amplify mRNA decapping by biasing enzyme conformation. Nat Chem Biol *17*, 615–623.
881 10.1038/s41589-021-00774-x.

882 20. Moon, S.L., Morisaki, T., Khong, A., Lyon, K., Parker, R., and Stasevich, T.J. (2019). Multicolour
883 single-molecule tracking of mRNA interactions with RNP granules. Nat Cell Biol *21*, 162–168.
884 10.1038/s41556-018-0263-4.

885 21. Pitchiaya, S., Mourao, M.D.A., Jalihal, A.P., Xiao, L., Jiang, X., Chinnaiyan, A.M., Schnell, S., and
886 Walter, N.G. (2019). Dynamic Recruitment of Single RNAs to Processing Bodies Depends on RNA
887 Functionality. Molecular Cell *74*, 521-533.e6. 10.1016/j.molcel.2019.03.001.

888 22. Hubstenberger, A., Courel, M., Bénard, M., Souquere, S., Ernoult-Lange, M., Chouaib, R., Yi, Z.,
889 Morlot, J.-B., Munier, A., Fradet, M., et al. (2017). P-Body Purification Reveals the Condensation of
890 Repressed mRNA Regulons. Molecular Cell *68*, 144-157.e5. 10.1016/j.molcel.2017.09.003.

891 23. Jain, S., Wheeler, J.R., Walters, R.W., Agrawal, A., Barsic, A., and Parker, R. (2016). ATPase-
892 Modulated Stress Granules Contain a Diverse Proteome and Substructure. Cell *164*, 487–498.
893 10.1016/j.cell.2015.12.038.

894 24. Khong, A., Matheny, T., Jain, S., Mitchell, S.F., Wheeler, J.R., and Parker, R. (2017). The Stress
895 Granule Transcriptome Reveals Principles of mRNA Accumulation in Stress Granules. Molecular Cell
896 *68*, 808-820.e5. 10.1016/j.molcel.2017.10.015.

897 25. Markmiller, S., Soltanieh, S., Server, K.L., Mak, R., Jin, W., Fang, M.Y., Luo, E.-C., Krach, F., Yang,
898 D., Sen, A., et al. (2018). Context-Dependent and Disease-Specific Diversity in Protein Interactions
899 within Stress Granules. Cell *172*, 590-604.e13. 10.1016/j.cell.2017.12.032.

900 26. Youn, J.-Y., Dunham, W.H., Hong, S.J., Knight, J.D.R., Bashkurov, M., Chen, G.I., Bagci, H., Rathod,
901 B., MacLeod, G., Eng, S.W.M., et al. (2018). High-Density Proximity Mapping Reveals the Subcellular
902 Organization of mRNA-Associated Granules and Bodies. Molecular Cell *69*, 517-532.e11.
903 10.1016/j.molcel.2017.12.020.

904 27. Xing, W., Muhlrad, D., Parker, R., and Rosen, M.K. (2020). A quantitative inventory of yeast P
905 body proteins reveals principles of composition and specificity. eLife *9*, e56525. 10.7554/eLife.56525.

906 28. Currie, S.L., Xing, W., Muhlrad, D., Decker, C.J., Parker, R., and Rosen, M.K. (2022). Quantitative
907 reconstitution of yeast RNA processing bodies. 2022.08.13.503854. 10.1101/2022.08.13.503854.

908 29. Al-Husini, N., Tomares, D.T., Pfaffenberger, Z.J., Muthunayake, N.S., Samad, M.A., Zuo, T., Bitar,
909 O., Aretakis, J.R., Bharmal, M.-H.M., Gega, A., et al. (2020). BR-Bodies Provide Selectively Permeable
910 Condensates that Stimulate mRNA Decay and Prevent Release of Decay Intermediates. Molecular Cell
911 *78*, 670-682.e8. 10.1016/j.molcel.2020.04.001.

912 30. Muthunayake, N.S., Al-Husini, N., and Schrader, J.M. (2020). Differential Centrifugation to Enrich
913 Bacterial Ribonucleoprotein Bodies (BR bodies) from Caulobacter crescentus. STAR Protocols *1*,
914 100205. 10.1016/j.xpro.2020.100205.

915 31. Hardwick, S.W., Chan, V.S.Y., Broadhurst, R.W., and Luisi, B.F. (2011). An RNA degradosome
916 assembly in Caulobacter crescentus. Nucleic Acids Res *39*, 1449–1459. 10.1093/nar/gkq928.

917 32. Canestrari, J.G., Lasek-Nesselquist, E., Upadhyay, A., Rofaeil, M., Champion, M.M., Wade, J.T.,
918 Derbyshire, K.M., and Gray, T.A. (2020). Polycysteine-encoding leaderless short ORFs function as

919 cysteine-responsive attenuators of operonic gene expression in mycobacteria. Molecular
920 Microbiology *114*, 93–108. 10.1111/mmi.14498.

921 33. Mousseau, C.B., Pierre, C.A., Hu, D.D., and Champion, M.M. (2022). Miniprep assisted
922 proteomics (MAP) for rapid proteomics sample preparation. Anal. Methods, 10.1039.D2AY01549H.
923 10.1039/D2AY01549H.

924 34. Voss, J.E., Luisi, B.F., and Hardwick, S.W. (2014). Molecular recognition of RhlB and RNase D in
925 the Caulobacter crescentus RNA degradosome. Nucleic Acids Research *42*, 13294–13305.
926 10.1093/nar/gku1134.

927 35. Aguirre, A.A., Vicente, A.M., Hardwick, S.W., Alvelos, D.M., Mazzon, R.R., Luisi, B.F., and
928 Marques, M.V. (2017). Association of the Cold Shock DEAD-Box RNA Helicase RhlE to the RNA
929 Degradosome in Caulobacter crescentus. Journal of Bacteriology *199*, e00135-17. 10.1128/JB.00135-
930 17.

931 36. Ghosh, A., Bharmal, M.-H.M., Ghaleb, A.M., Nandana, V., and Schrader, J.M. (2023). Initiator
932 AUGs Are Discriminated from Elongator AUGs Predominantly through mRNA Accessibility in C.
933 crescentus. Journal of Bacteriology *205*, e00420-22. 10.1128/jb.00420-22.

934 37. Russell, J.H., and Keiler, K.C. (2009). Subcellular localization of a bacterial regulatory RNA.
935 Proceedings of the National Academy of Sciences *106*, 16405–16409. 10.1073/pnas.0904904106.

936 38. Holmes, J.A., Follett, S.E., Wang, H., Meadows, C.P., Varga, K., and Bowman, G.R. (2016).
937 Caulobacter PopZ forms an intrinsically disordered hub in organizing bacterial cell poles. Proceedings
938 of the National Academy of Sciences *113*, 12490–12495. 10.1073/pnas.1602380113.

939 39. Aretakis, J.R., Gega, A., and Schrader, J.M. (2019). Absolute Measurements of mRNA Translation
940 in Caulobacter crescentus Reveal Important Fitness Costs of Vitamin B12 Scavenging. mSystems *4*,
941 e00170-19. 10.1128/mSystems.00170-19.

942 40. Hondele, M., Sachdev, R., Heinrich, S., Wang, J., Vallotton, P., Fontoura, B.M.A., and Weis, K.
943 (2019). DEAD-box ATPases are global regulators of phase-separated organelles. Nature *573*, 144–148.
944 10.1038/s41586-019-1502-y.

945 41. Beaufay, F., Amemiya, H.M., Guan, J., Basalla, J., Meinen, B.A., Chen, Z., Mitra, R., Bardwell,
946 J.C.A., Biteen, J.S., Vecchiarelli, A.G., et al. (2021). Polyphosphate drives bacterial heterochromatin
947 formation. Science Advances *7*, eabk0233. 10.1126/sciadv.abk0233.

948 42. Karimova, G., Pidoux, J., Ullmann, A., and Ladant, D. (1998). A bacterial two-hybrid system based
949 on a reconstituted signal transduction pathway. Proceedings of the National Academy of Sciences *95*,
950 5752–5756. 10.1073/pnas.95.10.5752.

951 43. Thanbichler, M., Iniesta, A.A., and Shapiro, L. (2007). A comprehensive set of plasmids for
952 vanillate- and xylose-inducible gene expression in Caulobacter crescentus. Nucleic Acids Res. *35*,
953 e137. 10.1093/nar/gkm818.

954 44. Krypotou, E., Townsend, G.E., Gao, X., Tachiyama, S., Liu, J., Pokorzynski, N.D., Goodman, A.L.,
955 and Groisman, E.A. (2023). Bacteria require phase separation for fitness in the mammalian gut.
956 Science *379*, 1149–1156. 10.1126/science.abn7229.

957 45. Tauber, D., Tauber, G., Khong, A., Van Treeck, B., Pelletier, J., and Parker, R. (2020). Modulation
958 of RNA Condensation by the DEAD-Box Protein eIF4A. Cell *180*, 411-426.e16.
959 10.1016/j.cell.2019.12.031.

960 46. Assis, N.G., Ribeiro, R.A., Silva, L.G. da, Vicente, A.M., Hug, I., and Marques, M.V. (2019).
961 Identification of Hfq-binding RNAs in Caulobacter crescentus. RNA Biology *16*, 719–726.
962 10.1080/15476286.2019.1593091.

963 47. Møller, T., Franch, T., Højrup, P., Keene, D.R., Bächinger, H.P., Brennan, R.G., and Valentin-
964 Hansen, P. (2002). Hfq: A Bacterial Sm-like Protein that Mediates RNA-RNA Interaction. Molecular
965 Cell *9*, 23–30. 10.1016/S1097-2765(01)00436-1.

966 48. Updegrove, T.B., Zhang, A., and Storz, G. (2016). Hfq: the flexible RNA matchmaker. Curr Opin
967 Microbiol *30*, 133–138. 10.1016/j.mib.2016.02.003.

968 49. Urban, J.H., and Vogel, J. (2008). Two Seemingly Homologous Noncoding RNAs Act Hierarchically
969 to Activate glmS mRNA Translation. PLOS Biology *6*, e64. 10.1371/journal.pbio.0060064.

970 50. Vogel, J., and Luisi, B.F. (2011). Hfq and its constellation of RNA. Nat Rev Microbiol *9*, 578–589.
971 10.1038/nrmicro2615.

972 51. Ikeda, Y., Yagi, M., Morita, T., and Aiba, H. (2011). Hfq binding at RhlB-recognition region of
973 RNase E is crucial for the rapid degradation of target mRNAs mediated by sRNAs in Escherichia coli.
974 Molecular Microbiology *79*, 419–432. 10.1111/j.1365-2958.2010.07454.x.

975 52. Fei, J., Singh, D., Zhang, Q., Park, S., Balasubramanian, D., Golding, I., Vanderpool, C.K., and Ha,
976 T. (2015). Determination of in vivo target search kinetics of regulatory noncoding RNA. Science *347*,
977 1371–1374. 10.1126/science.1258849.

978 53. Duval, M., Korepanov, A., Fuchsbauer, O., Fechter, P., Haller, A., Fabbretti, A., Choulier, L.,
979 Micura, R., Klaholz, B.P., Romby, P., et al. (2013). Escherichia coli Ribosomal Protein S1 Unfolds
980 Structured mRNAs Onto the Ribosome for Active Translation Initiation. PLOS Biology *11*, e1001731.
981 10.1371/journal.pbio.1001731.

982 54. Delvillani, F., Papiani, G., Dehò, G., and Briani, F. (2011). S1 ribosomal protein and the interplay
983 between translation and mRNA decay. Nucleic Acids Res *39*, 7702–7715. 10.1093/nar/gkr417.

984 55. Robledo, M., García-Tomsig, N.I., Matia-González, A.M., García-Rodríguez, F.M., and Jiménez-
985 Zurdo, J.I. (2021). Synthetase of the methyl donor S-adenosylmethionine from nitrogen-fixing α-
986 rhizobia can bind functionally diverse RNA species. RNA Biology *18*, 1111–1123.
987 10.1080/15476286.2020.1829365.

988 56. Britos, L., Abeliuk, E., Taverner, T., Lipton, M., McAdams, H., and Shapiro, L. (2011). Regulatory
989 Response to Carbon Starvation in Caulobacter crescentus. PLOS ONE *6*, e18179.
990 10.1371/journal.pone.0018179.

991 57. Cabrera, J.E., Cagliero, C., Quan, S., Squires, C.L., and Jin, D.J. (2009). Active Transcription of
992 rRNA Operons Condenses the Nucleoid in Escherichia coli: Examining the Effect of Transcription on
993 Nucleoid Structure in the Absence of Transertion. Journal of Bacteriology *191*, 4180–4185.
994 10.1128/JB.01707-08.

995 58. Queiroz, R.M.L., Smith, T., Villanueva, E., Marti-Solano, M., Monti, M., Pizzinga, M., Mirea, D.-
996 M., Ramakrishna, M., Harvey, R.F., Dezi, V., et al. (2019). Comprehensive identification of RNA–
997 protein interactions in any organism using orthogonal organic phase separation (OOPS). Nat
998 Biotechnol *37*, 169–178. 10.1038/s41587-018-0001-2.

999 59. Shchepachev, V., Bresson, S., Spanos, C., Petfalski, E., Fischer, L., Rappsilber, J., and Tollervey, D.
1000 (2019). Defining the RNA interactome by total RNA-associated protein purification. Molecular
1001 Systems Biology *15*, e8689. 10.15252/msb.20188689.

1002 60. Hentze, M.W., Castello, A., Schwarzl, T., and Preiss, T. (2018). A brave new world of RNA-binding
1003 proteins. Nat Rev Mol Cell Biol *19*, 327–341. 10.1038/nrm.2017.130.

1004 61. van Mierlo, G., Jansen, J.R.G., Wang, J., Poser, I., van Heeringen, S.J., and Vermeulen, M. (2021).
1005 Predicting protein condensate formation using machine learning. Cell Reports *34*, 108705.
1006 10.1016/j.celrep.2021.108705.

1007 62. Saar, K.L., Morgunov, A.S., Qi, R., Arter, W.E., Krainer, G., Lee, A.A., and Knowles, T.P.J. (2021).
1008 Learning the molecular grammar of protein condensates from sequence determinants and
1009 embeddings. Proceedings of the National Academy of Sciences *118*, e2019053118.
1010 10.1073/pnas.2019053118.

1011 63. Riback, J.A., Katanski, C.D., Kear-Scott, J.L., Pilipenko, E.V., Rojek, A.E., Sosnick, T.R., and
1012 Drummond, D.A. (2017). Stress-Triggered Phase Separation Is an Adaptive, Evolutionarily Tuned
1013 Response. Cell *168*, 1028-1040.e19. 10.1016/j.cell.2017.02.027.

1014 64. Evinger, M., and Agabian, N. (1977). Envelope-associated nucleoid from Caulobacter crescentus
1015 stalked and swarmer cells. Journal of Bacteriology *132*, 294–301. 10.1128/jb.132.1.294-301.1977.

1016 65. Schrader, J.M., and Shapiro, L. (2015). Synchronization of Caulobacter Crescentus for
1017 Investigation of the Bacterial Cell Cycle. JoVE (Journal of Visualized Experiments), e52633.
1018 10.3791/52633.

1019 66. Cronin, R.M., Ferrell, M.J., Cahir, C.W., Champion, M.M., and Champion, P.A. (2022). Proteo-
1020 genetic analysis reveals clear hierarchy of ESX-1 secretion in Mycobacterium marinum. Proceedings
1021 of the National Academy of Sciences *119*, e2123100119. 10.1073/pnas.2123100119.

1022 67. Vernon, R.M., Chong, P.A., Tsang, B., Kim, T.H., Bah, A., Farber, P., Lin, H., and Forman-Kay, J.D.
1023 (2018). Pi-Pi contacts are an overlooked protein feature relevant to phase separation. eLife *7*,
1024 e31486. 10.7554/eLife.31486.

1025 68. Ducret, A., Quardokus, E.M., and Brun, Y.V. (2016). MicrobeJ, a tool for high throughput
1026 bacterial cell detection and quantitative analysis. Nat Microbiol *1*, 1–7. 10.1038/nmicrobiol.2016.77.

1027 69. Postma, M., and Goedhart, J. (2019). PlotsOfData—A web app for visualizing data together with
1028 their summaries. PLOS Biology *17*, e3000202. 10.1371/journal.pbio.3000202.

1029 70. Jing, B., Xu, D., Wang, X., and Zhu, Y. (2018). Multiresponsive, Critical Gel Behaviors of
1030 Polyzwitterion–Polyoxometalate Coacervate Complexes. Macromolecules *51*, 9405–9411.
1031 10.1021/acs.macromol.8b01759.

1032 71. Sherman, B.T., Hao, M., Qiu, J., Jiao, X., Baseler, M.W., Lane, H.C., Imamichi, T., and Chang, W.
1033 (2022). DAVID: a web server for functional enrichment analysis and functional annotation of gene
1034 lists (2021 update). Nucleic Acids Research *50*, W216–W221. 10.1093/nar/gkac194.

1035 72. Romero, P., Obradovic, Z., Kissinger, C., Villafranca, J.E., and Dunker, A.K. (1997). Identifying
1036 disordered regions in proteins from amino acid sequence. In Proceedings of International Conference
1037 on Neural Networks (ICNN'97), pp. 90–95 vol.1. 10.1109/ICNN.1997.611643.

1038 73. Bolognesi, B., Lorenzo Gotor, N., Dhar, R., Cirillo, D., Baldrighi, M., Tartaglia, G.G., and Lehner, B.
1039 (2016). A Concentration-Dependent Liquid Phase Separation Can Cause Toxicity upon Increased
1040 Protein Expression. Cell Reports *16*, 222–231. 10.1016/j.celrep.2016.05.076.

1041

Figure 1

A.

BR-body enrichment assay

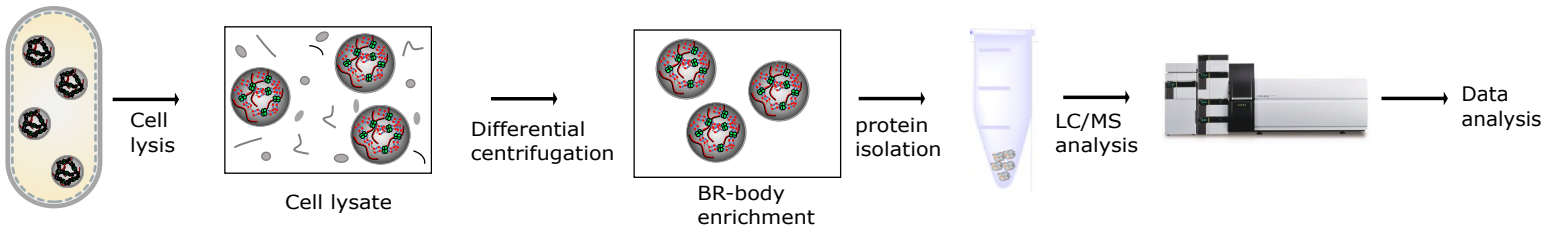

B.

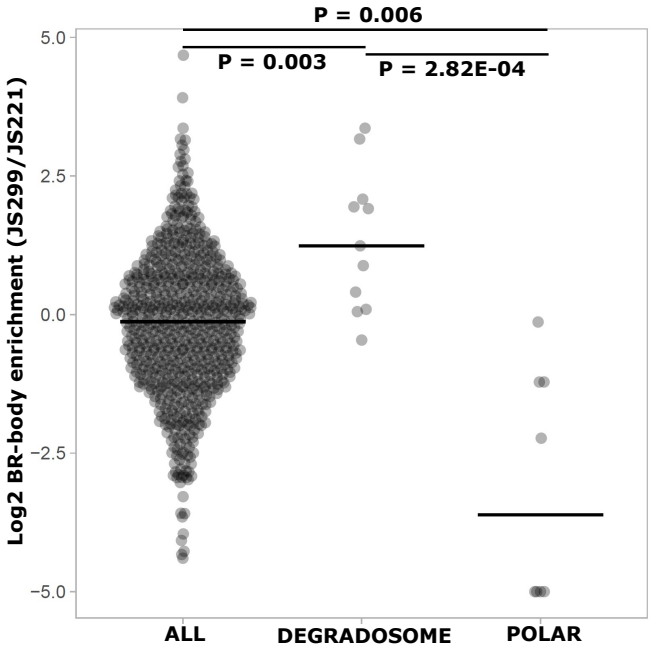

Enriched	Number of proteins	p-value
Cytoplasm	32	9.40E-11
Depleted		
Membrane	160	3.90E-23
Transmembrane	126	2.30E-12
Cell inner membrane	33	3.00E-12
Transmembrane helix	121	3.80E-11
Cell membrane	40	4.30E-11
Cell outer membrane	7	1.30E-03
Cell wall	5	6.40E-02

Enriched	Number of proteins	p-value
RNA Binding	14	9.00E-07
ATP Binding	19	8.80E-03
RNA Degradation	5	9.90E-03
GTPase Activity	5	3.80E-03

Figure 2

A.

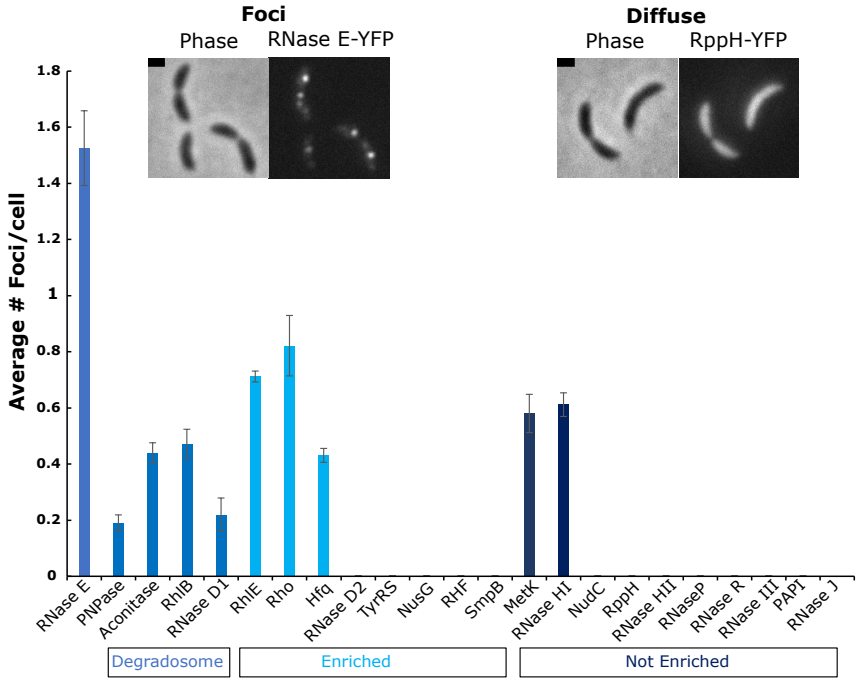

B.

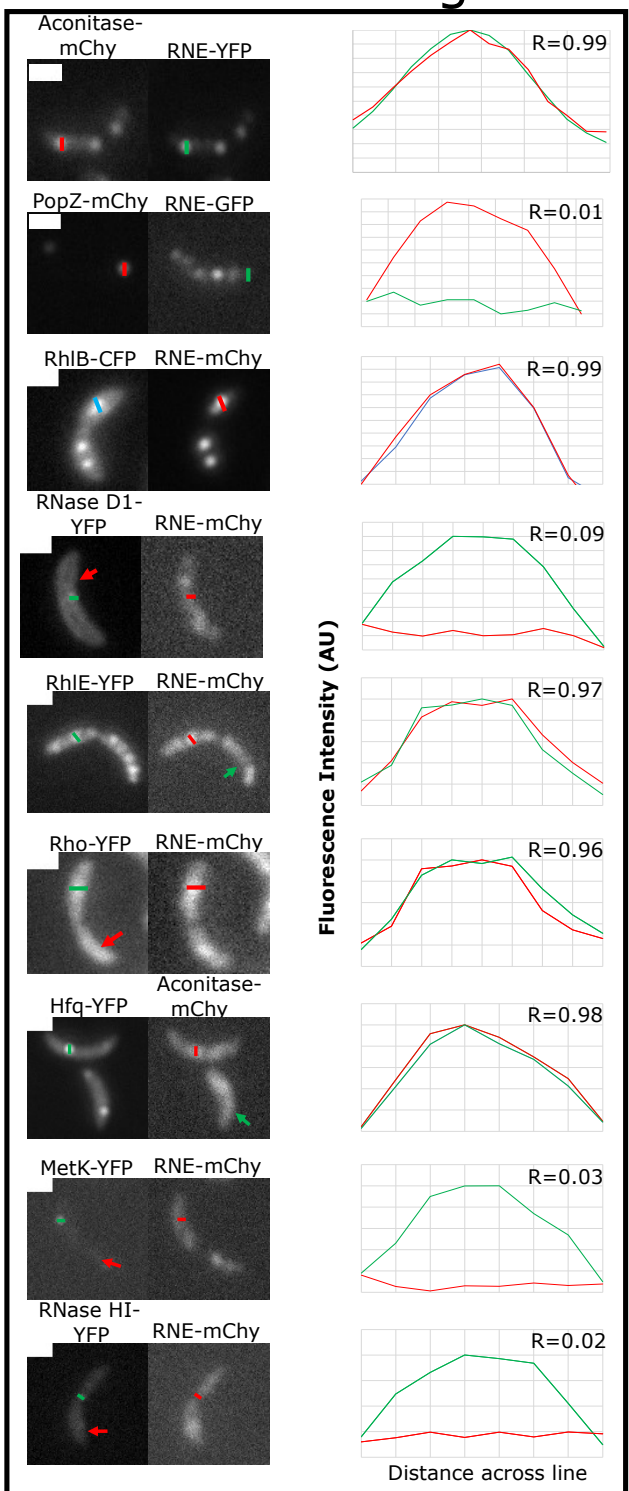

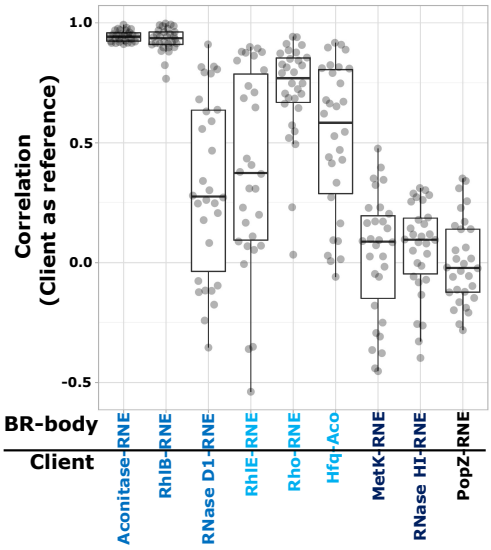

C.

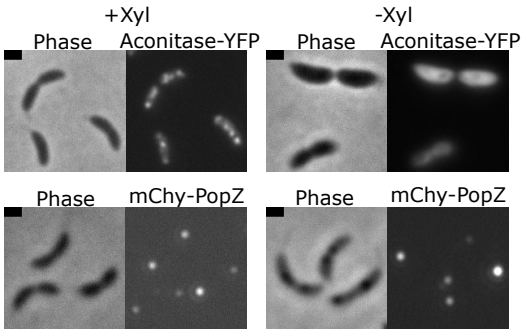

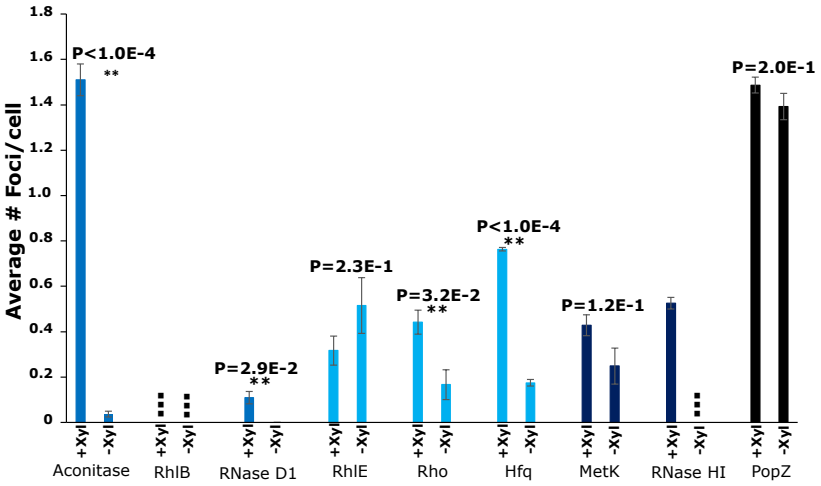

D.

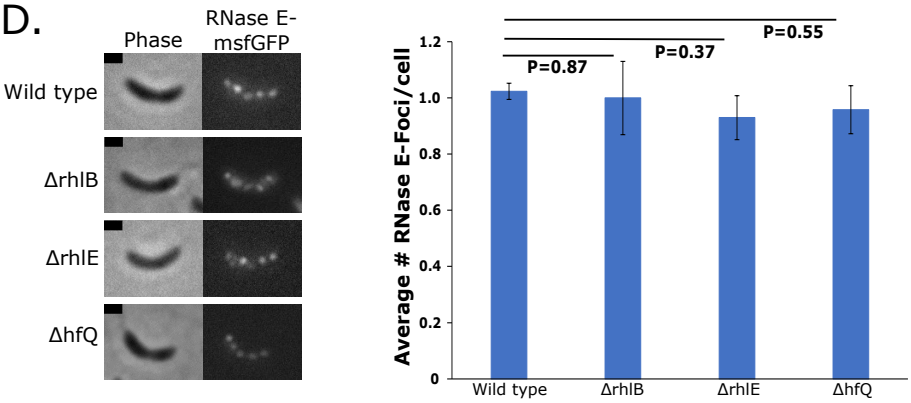

Figure 3

A.

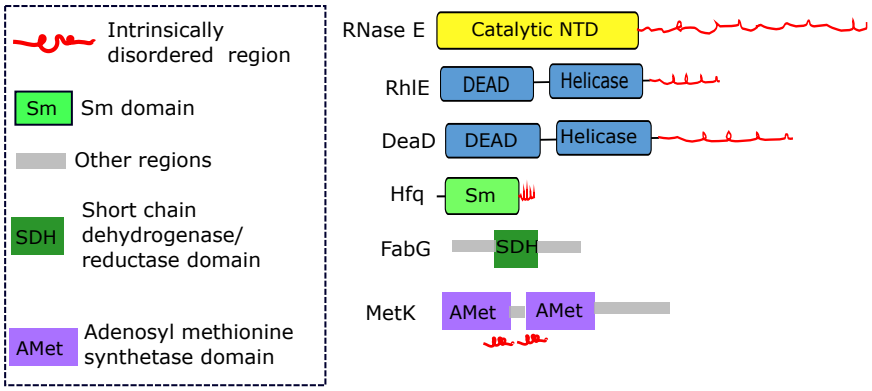

Protein	Disorderness %	Pscore	Catgranule	Deephase
RNase E	35.9	3.72	1.26	0.79
RhlE	17.23	1.29	1.04	0.58
DEAD	32.79	4.48	1.04	0.76
Hfq	0	-0.83	-1.06	0.1
FabG	0	-0.02	0.96	0.1
MetK	0	0.15	-0.068	0.22

B.

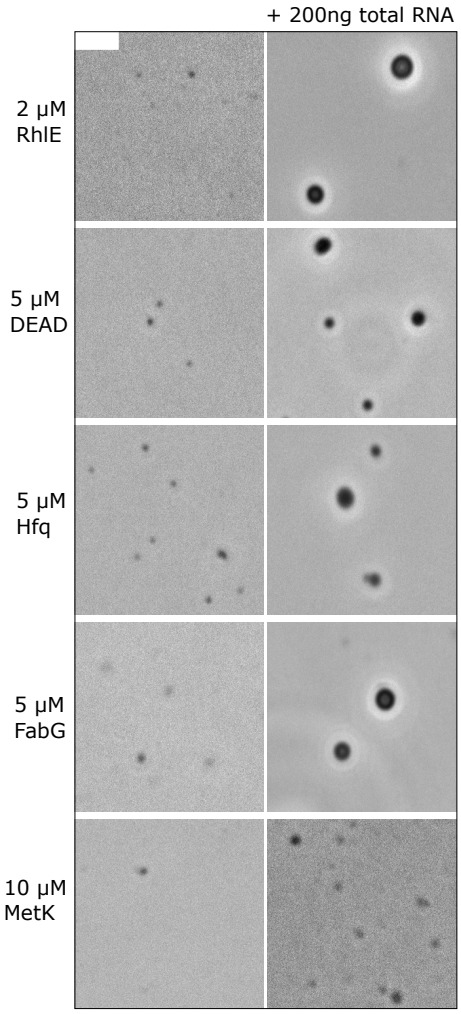

C.

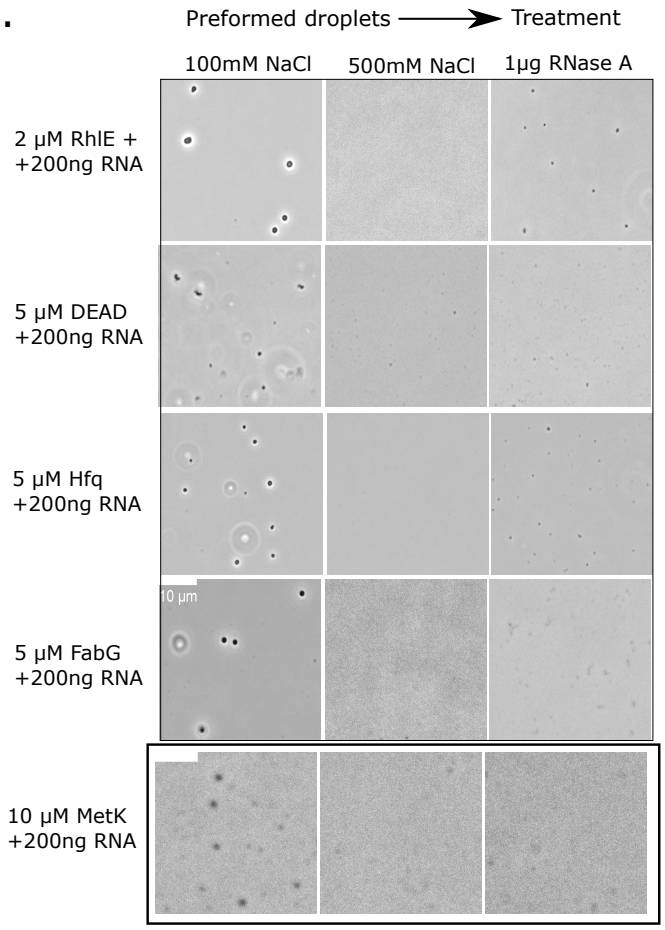

Figure 4

A.

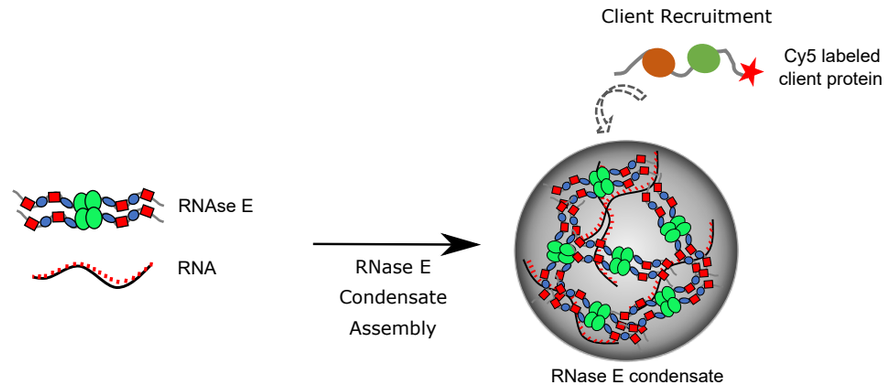
Client Recruitment
Cy5 labeled
client protein
RNAse E
RNA
RNase E
Condensate
Assembly
RNase E condensate

B.

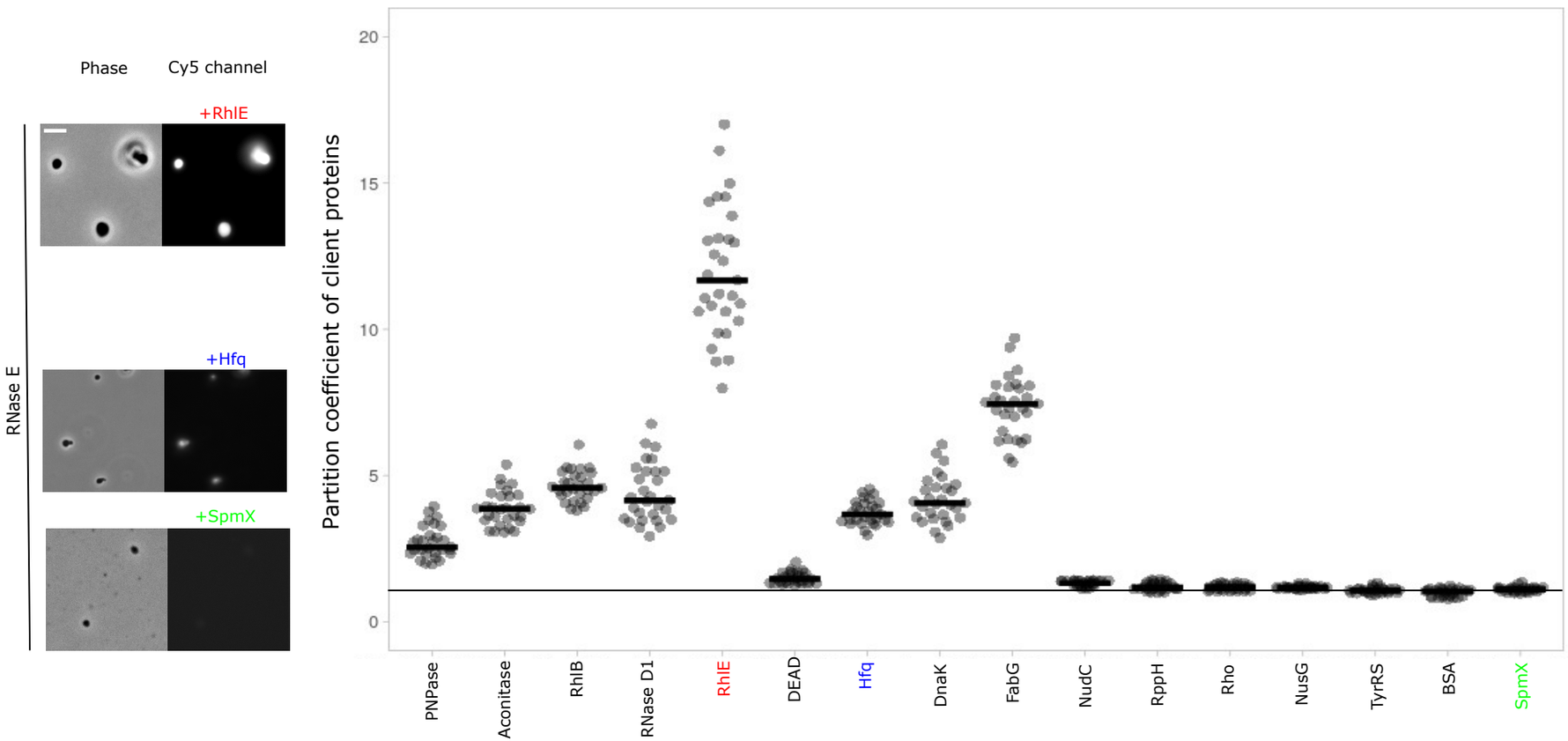
Phase
Cy5 channel
+RhlE
+Hfq
+SpmX
RNase E
Partition coefficient of client proteins
20
15
10
5
0
PNPase
Aconitase
RhlB
RNase D1
RhlE
DEAD
Hfq
DnaK
FabG
NudC
RppH
Rho
NusG
TyrRS
BSA
SpmX

Figure 5

A. **Droplet Dissolution**

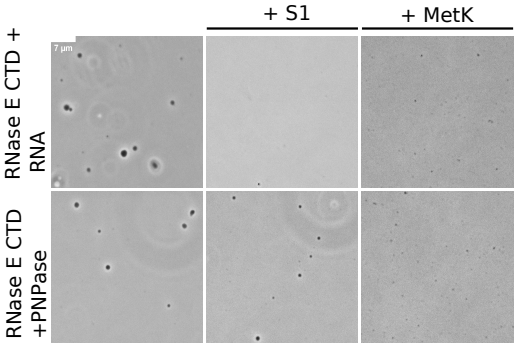

B. **RNA binding**

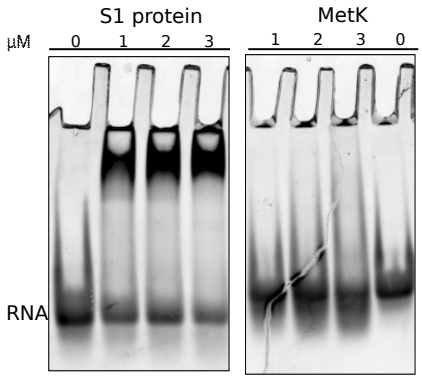

C. **Affinity co-precipitation**

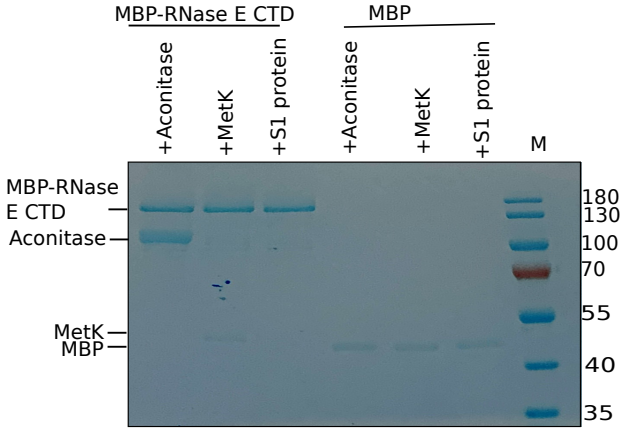

D. **Bacterial 2-hybrid**

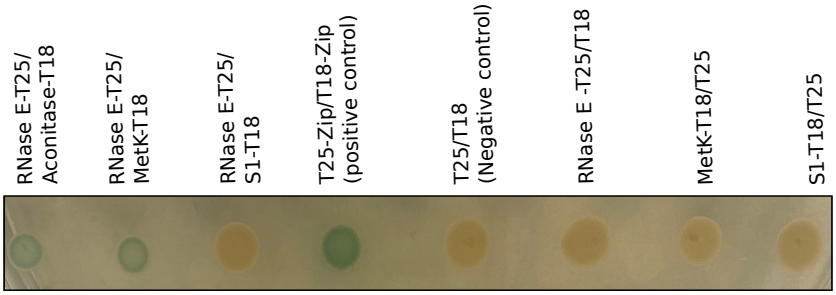

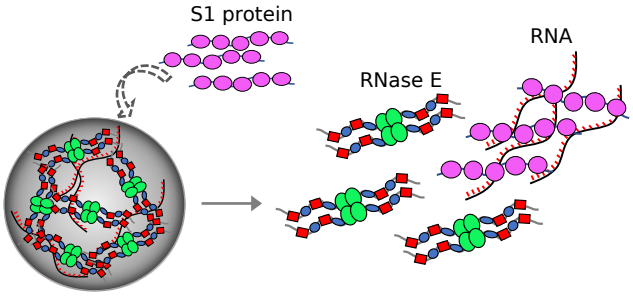

S1 protein dissolution occurs via RNA binding

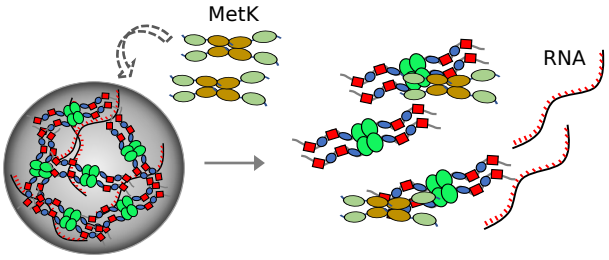

MetK dissolution occurs via RNase E binding

E. ***In vivo* dissolution**

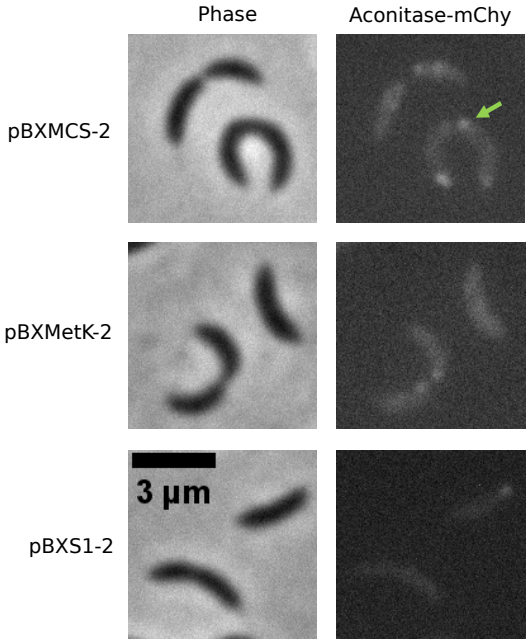

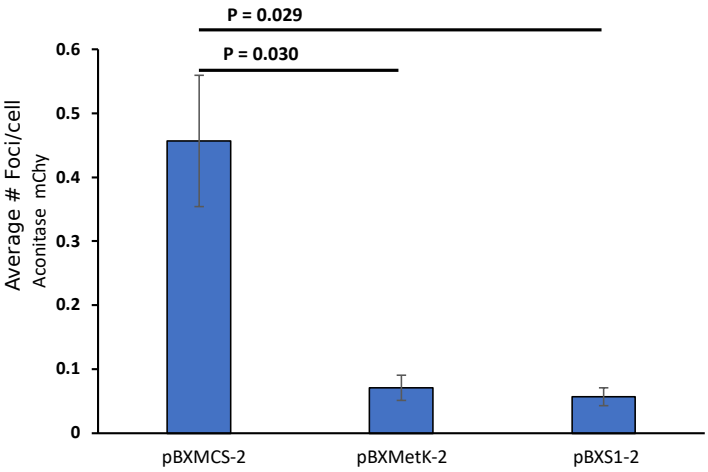

Figure 6

A.

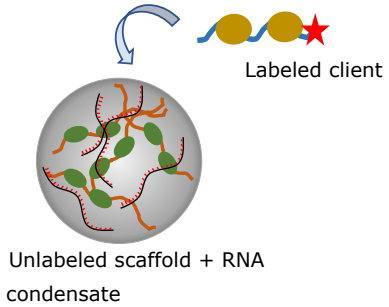

Labeled client

Scaffold	RhlB	PNP	Aco	RNase D1
RNase E	4.7	2.6	4	4
RhlE	1.0	1.0	1.0	1.0
DEAD	1.5	1.5	1.5	1.5
Hfq	2.3	1.7	2.5	1.7
FabG	1.5	1.7	1.5	1.6

Partition Coefficient

15	High
10	
5	
1	Low

B.

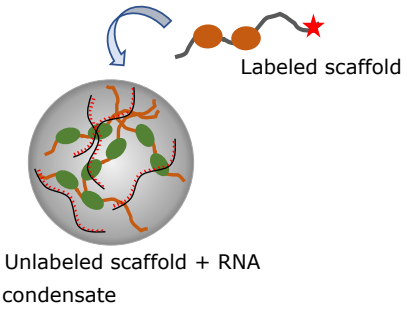

Labeled Scaffold

Scaffold	RNase E	RhlE	DEAD	Hfq	FabG
RNase E	X	11	1.5	7.5	3.8
RhlE	1.6	X	1.5	2.5	2.5
DEAD	1.7	7.6	X	3.3	2.6
Hfq	ND	4.3	1.8	X	2.4
FabG	1.9	7.4	1.5	3.4	X

C.

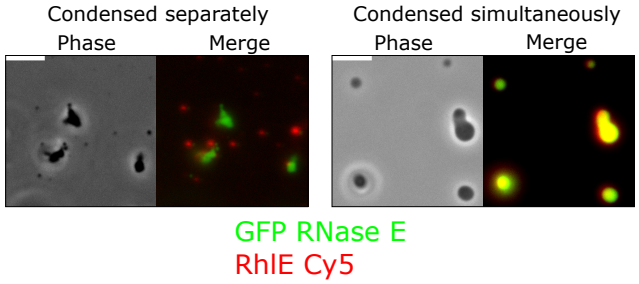

D.

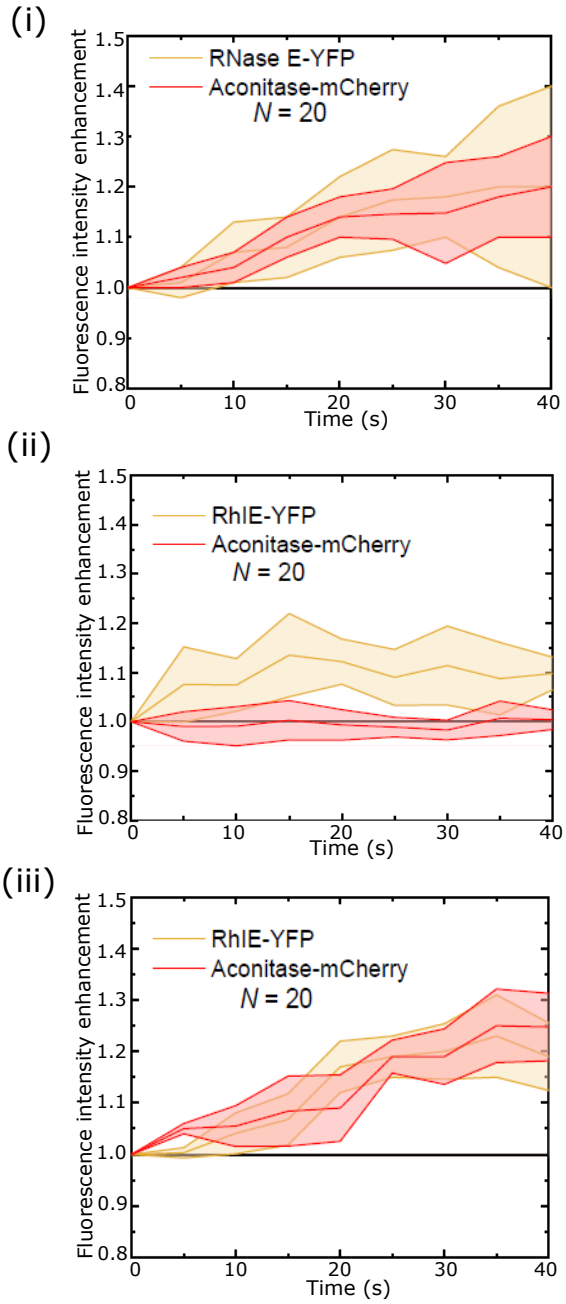

Figure 7

A.

Kinetics of RNase E Condensation

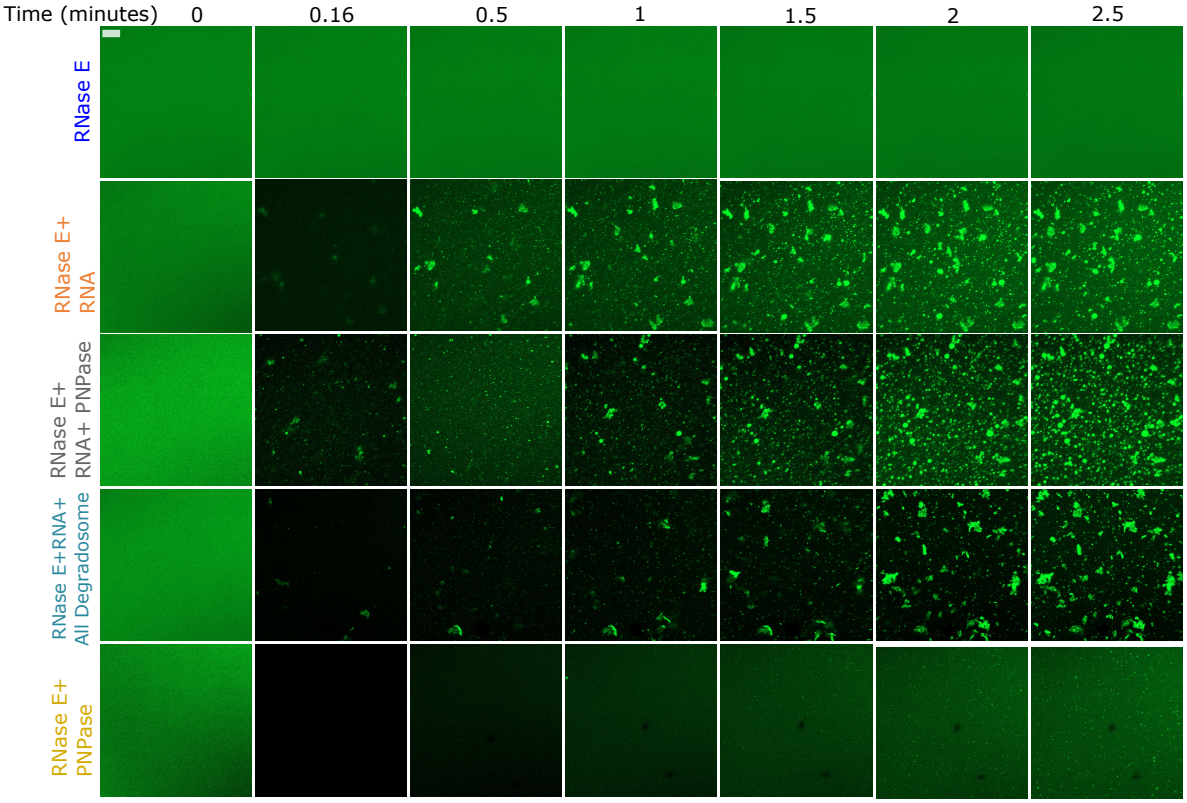

B.

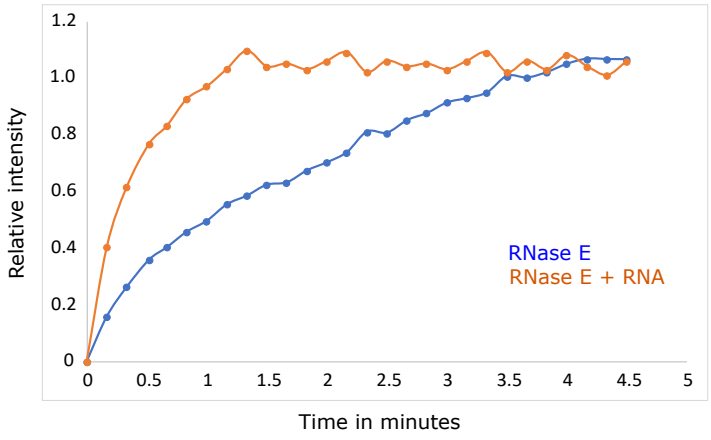
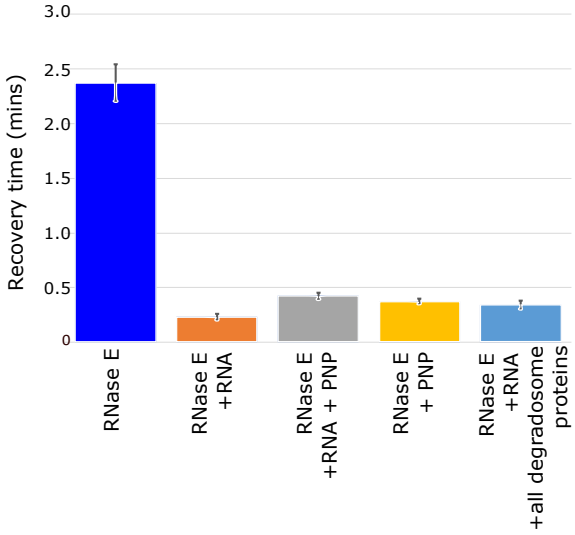
C.